

Frazil ice growth and production during katabatic wind events in the Ross Sea, Antarctica

1 Lisa De Pace¹, Madison Smith², Jim Thomson², Sharon Stammerjohn³, Steve Ackley⁴, and Brice
2 Loose⁵

3

4 ¹Department of Science, US Coast Guard Academy, New London CT

5 ²Applied Physics Laboratory, University of Washington, Seattle WA

6 ³Institute for Arctic and Alpine Research, University of Colorado at Boulder, Boulder CO

7 ⁴University of Texas at San Antonio, San Antonio TX

8 ⁵Graduate School of Oceanography, University of Rhode Island, Narragansett RI

9

10 *Correspondence to:* Brice Loose (bloose@uri.edu)

11

12 **ABSTRACT:** During katabatic wind events in the Terra Nova Bay and Ross Sea polynyas, wind
13 speeds exceeded 20 m s^{-1} , air temperatures were below $-25 \text{ }^{\circ}\text{C}$, and the mixed layer extended as
14 deep as 600 meters. Yet, upper ocean temperature and salinity profiles were not perfectly
15 homogeneous, as would be expected with vigorous convective heat loss. Instead, the profiles
16 revealed bulges of warm and salty water directly beneath the ocean surface and extending
17 downwards tens of meters. Considering both the colder air above and colder water below, we
18 suggest the increase in temperature and salinity reflects latent heat and salt release during
19 unconsolidated frazil ice production within the upper water column. We use a simplified salt
20 budget to analyze these anomalies to estimate in-situ frazil ice concentration between 266×10^{-3}
21 and $13 \times 10^{-3} \text{ kg m}^{-3}$. Contemporaneous estimates of vertical mixing by turbulent kinetic energy
22 dissipation reveal rapid convection in these unstable density profiles, and mixing lifetimes from
23 7 to 12 minutes. The corresponding frazil ice production rates covary with wind speed and with
24 location along the upstream-downstream length of the polynya. The individual estimates of ice
25 production from the salt budget reveal the intensity of short-term ice production, up to 110 cm
26 day^{-1} during the windiest events, but they scale to a seasonal average of 29 cm day^{-1} . These
27 measurements suggest that frazil ice may be an important component in polynya ice production.

28

29

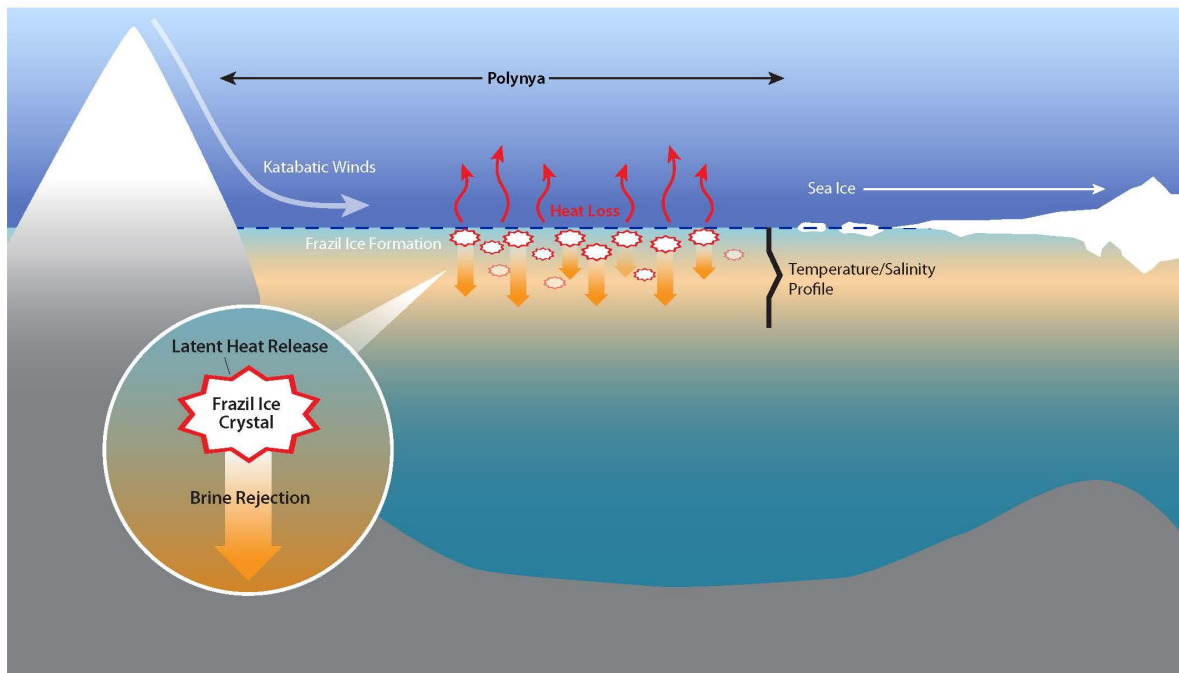
30

31 1. INTRODUCTION

32

33 Latent heat polynyas form in areas where prevailing winds or oceanic currents create
34 divergence in the ice cover, leading to openings either surrounded by extensive pack ice or
35 bounded by land on one side and pack ice on the other (coastal polynyas) (Armstrong, 1972;
36 Park et al, 2018). The open water of polynyas is critical for air-sea heat exchange, since ice
37 covered waters are better insulated and reduce the amount of heat flux to the atmosphere (Fusco
38 et al., 2009; Talley et al, 2011). A key feature of coastal or latent heat polynyas are katabatic
39 winds (Figure 1), which originate as cold, dense air masses that form over the continental ice
40 sheets of Antarctica. These air masses flow as sinking gravity currents, descending off the
41 glaciated continent, or in the case of the Terra Nova Bay Polynya, through the Transantarctic
42 mountain range. These flows are often funneled and strengthened by mountain-valley
43 topography. The katabatic winds create and maintain latent heat polynyas. This research focuses
44 on in-situ measurements taken from two coastal latent heat polynyas in the Ross Sea, the Terra
45 Nova Bay polynya and the Ross Sea polynya.

46



47

48 Figure 1: Schematic of a latent heat or coastal polynya. The polynya is kept open from katabatic
49 winds which drive ice advection, oceanic heat loss and frazil ice formation. Ice formation results
50 in oceanic loss of latent heat to the atmosphere and brine rejection. Inset is a schematic of Frazil
51 ice formation that depicts the release of latent heat of fusion and brine rejection as a frazil ice
52 crystal is formed.

53

54 The extreme oceanic heat loss in polynyas can generate supercooled water, which is
55 colder than the freezing point (Skogseth et al., 2009; Dmitrenko et al, 2010; Matsumura &
56 Ohshima, 2015), and is the precursor to ice nucleation. In turbulent, supercooled water sea ice
57 formation begins with fine disc-shaped or dendritic crystals called frazil ice. These frazil ice
58 crystals (Figure 1 inset) are about 1 to 4 mm in diameter and 1-100 μm thick (Martin, 1981). In
59 polynyas, the frazil ice is transported downwind from the formation site and can mix over a
60 region of 5-15 meters depth (Heorton et al, 2017; Ito et al, 2015). Katabatic winds sustain the
61 polynya by clearing frazil ice, forming pancake ice which piles up at the polynya edge to form a
62 consolidated ice cover (Morales Maqueda et al, 2004; Ushio and Wakatsuchi, 1993, Wilchinsky
63 et al, 2015).

64 Brine rejection (Cox & Weeks, 1983) during ice production, can lead to dense water
65 formation (Ohshima et al, 2016). Over the Antarctic continental shelf, this process produces a
66 water mass known as High Salinity Shelf Water (HSSW) (Talley et al, 2011). In the case of the
67 Ross Sea, the cold, dense HSSW formed on the shelf eventually becomes Antarctic Bottom
68 Water (AABW) off the shelf, the densest water in the abyssal ocean (Cosimo & Gordon, 1998;
69 Jacobs, 2004; Martin, et al., 2007; Tamura et al.; 2008). Terra Nova Bay polynya produces
70 especially dense HSSW, and produces approximately 1-1.5 Sv of HSSW annually (Buffoni et al.,
71 2002; Orsi & Wiederwohl, 2009; Sansivero et al, 2017; Van Woert 1999a,b).

72 Given the importance of AABW to meridional overturning circulation, polynya ice
73 production rates have been intensively studied. Gallee (1997), Petrelli et al. (2008), Fusco et al.
74 (2002), and Sansivero et al. (2017) used models to calculate polynya ice production rates on the
75 order of tens of centimeters per day. Schick (2018) and Kurtz and Bromwich (1985) used heat
76 fluxes to estimate polynya ice production rates, also on the order of tens of centimeters per day.
77 Drucker et al (2011), Ohshima et al (2016) Nihasi and Oshima (2015), and Tamura et al (2016)
78 used satellite remote sensing and microwave sensors to estimate annual production rates on the

79 order of tens of kilometers cubed per year. However, the heterogeneous and disaggregated
80 process of ice formation, which occurs on scales of μm , and accumulates over km, in very harsh
81 observational conditions makes it difficult to direct measurements that can lead to better
82 mechanistic predictions (Fusco et al., 2009; Tamura et al., 2008).

83

84 **1.2 Motivation for this article**

85 Late autumn CTD profiles from the Ross Sea coastal polynyas revealed anomalous bulges of
86 warmer, saltier water near the ocean surface during katabatic wind events. During these events,
87 we observed wind rows of frazil ice aggregation. We hypothesized that the excess temperature
88 was evidence of latent heat of release during frazil ice formation, and the excess salinity was
89 evidence of brine rejection from the same. We attempt to validate and confirm these
90 observations by comparing the shape and size of the profile anomalies with estimates of the CTD
91 precision and stability, and by using supporting evidence of the atmospheric conditions that are
92 thought to drive frazil ice formation (e.g. temperature and wind speed). This analysis is described
93 below, followed by our estimates of frazil ice concentration using the temperature and salinity
94 anomalies (§4). To better understand the importance of frazil formation, we computed the
95 lifetime of these anomalies (§5), which in turn yielded frazil ice production rates (§6). Last, we
96 discuss the implications for spatial variability of ice production and application for further
97 polynya sea ice production estimates.

98

99

100 **2. STUDY AREA AND DATA**

101

102 **2.1 The Terra Nova Bay Polynya and Ross Sea Polynya**

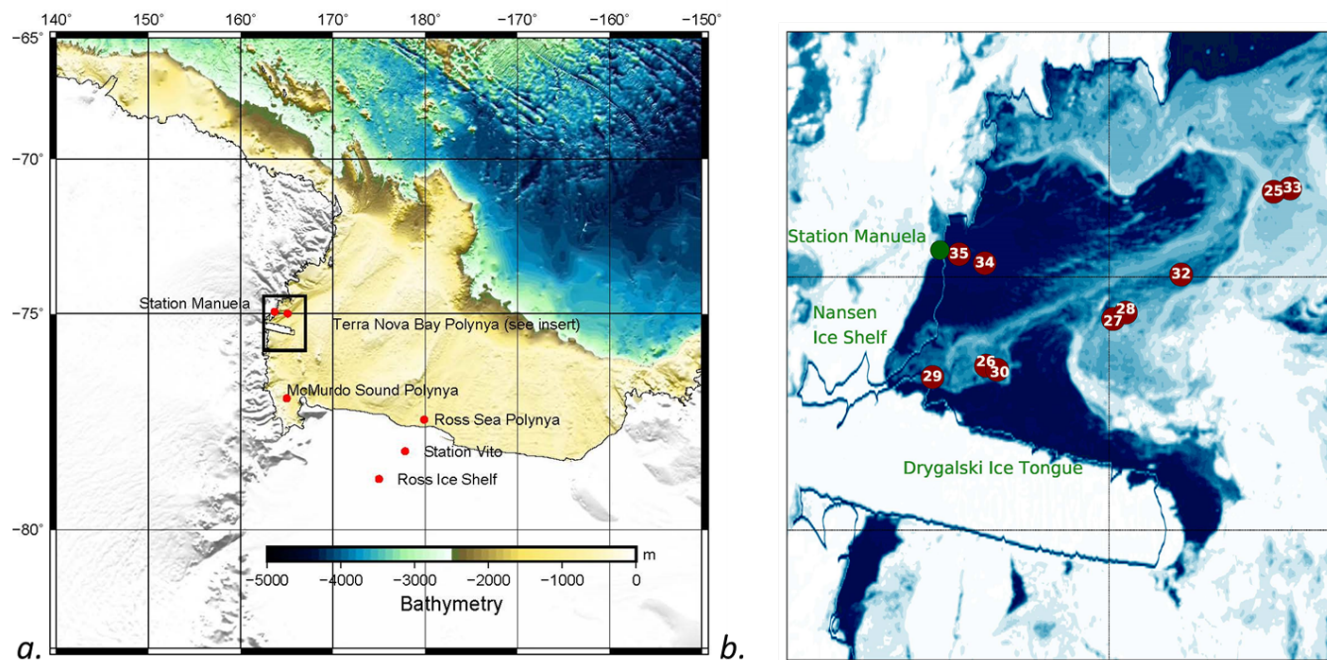
103

104 The Ross Sea, a southern extension of the Pacific Ocean, abuts Antarctica along the
105 Transantarctic Mountains and has three recurring latent heat polynyas: Ross Sea polynya (RSP),
106 Terra Nova Bay polynya (TNBP), and McMurdo Sound polynya (MSP) (Martin et al., 2007).
107 The RSP is Antarctica's largest recurring polynya, the average area of the RSP is 27,000 km² but
108 can grow as large as 50,000 km² depending on environmental conditions (Morales Maqueda, et
109 al., 2004; Park et al, 2018). It is located in the central and western Ross Sea to the east of Ross

110 Island, adjacent to the Ross Ice Shelf (Figure 2), and typically extends the entire length of the
111 Ross Ice Shelf (Martin et al., 2007; Morales Maqueda et al., 2004). TNBP is bounded to the
112 south by the Drygalski ice tongue, which serves to control the polynya maximum size (Petrelli et
113 al., 2008). TNBP and MSP, the smallest of the three polynyas, are both located in the western
114 Ross Sea (Figure 2). The area of TNBP, on average is 1300 km², but can extend up to 5000 km²;
115 the oscillation period of TNBP broadening and contracting is 15-20 days (Bromwich & Kurtz,
116 1984). This paper focuses primarily on TNBP and secondarily on RSP, where our observations
117 were taken.

118 During the autumn and winter season, Morales Maqueda et al., (2004) estimated TNBP
119 cumulative ice production to be around 40-60 meters of ice, or approximately 10% of the annual
120 sea ice production that occurs on the Ross Sea continental shelf. The RSP has a lower daily ice
121 production rate, but produces three to six times as much as TNBP annually due to its much larger
122 size (Petrelli et al., 2008).

123



124

125 Figure 2: Map of the Ross Sea and the Terra Nova Bay Polynya. a) Overview of the Ross Sea,
126 Antarctica highlighting the locations of the three recurring polynyas: Ross Sea Polynya (RSP),
127 Terra Nova Bay Polynya (TNBP), and McMurdo Sound Polynya (MSP). Bathymetry source:
128 GEBCO 1-degree grid. b) Terra Nova Bay Polynya Insert as indicated by black box in panel a.

129 MODIS image of TNBP with the 10 CTD stations with anomalies shown. Not included is CTD
130 Station 40, the one station with an anomaly located in the RSP. (CTD Station 40 is represented
131 on Figure 2a as the location of the Ross Sea Polynya.) Date of MODIS image is March 13,
132 2017; MODIS from during cruise dates could not be used due to the lack of daylight and high
133 cloud cover.

134

135 **2.2 PIPERS Expedition**

136 We collected this data during late autumn, from April 11 to June 14, 2017 aboard the
137 RVIB Nathaniel B. Palmer (NB Palmer, NBP17-04). More information about the research
138 activities during the PIPERS expedition is available at
139 <http://www.utsa.edu/signl/pipers/index.html>. Vertical profiles of Conductivity, Temperature, and
140 Depth (CTD) were taken at 58 stations within the Ross Sea. For the purposes of this study, we
141 focus on the 13 stations (CTD 23-35) that occurred within the TNBP and 4 stations (CTD 37-40)
142 within the RSP during katabatic wind events (Figure 2). In total, 11 of these 17 polynya stations
143 will be selected for use in our analysis, as described in §3.1. CTD station numbers follow the
144 original enumeration used during NBP17-04, so they are more easily traceable to the
145 hydrographic data, which is archived as described below in the Data Availability section.

146

147 **2.3 CTD measurements**

148 The CTD profiles were carried out using a Seabird 911 CTD (SBE 911) attached to a 24
149 bottle CTD rosette, which is supported and maintained by the Antarctic Support Contract (ASC).
150 Between CTD casts, the SBE911 was stored at room temperature to avoid freezing components.
151 Before each cast, the CTD was soaked at approximately 10 meters for 3-6 minutes until the
152 spikes in the conductivity readings ceased, suggesting the pump had purged all air bubbles from
153 the conductivity cell. Each CTD cast contains both down and up cast profiles. In many instances,
154 the upcast recorded a similar thermal and haline anomaly. However, the 24 bottle CTD rosette
155 package creates a large wake that disturbs the readings on the up cast leading to some profiles
156 with missing data points and more smoothed profiles, so only the wake uncontaminated down
157 cast profiles are used (Supplemental Figure 1 offers a comparison of the up vs down casts).

158 The instrument resolution is important for this study, because the anomalous profiles
159 were identified by comparing the near surface CTD measurements with other values within the

160 same profiles. The reported initial accuracy for the SBE 911 is $\pm 0.0003 \text{ S m}^{-1}$, $\pm 0.001 \text{ }^\circ\text{C}$, and
161 0.015% of the full-scale range of pressure for conductivity, temperature, and depth respectively.
162 Independent of the accuracy stated above, the SBE 911 can resolve differences in conductivity,
163 temperature, and pressure on the order of 0.00004 S m^{-1} , $0.0002 \text{ }^\circ\text{C}$ and 0.001% of the full range,
164 respectively (SeaBird Scientific, 2018). The SBE 911 samples at 24 Hz with an e-folding time
165 response of 0.05 seconds for conductivity and temperature. The time response for pressure is
166 0.015 seconds.

167 The SBE 911 data were processed using post-cruise calibrations by Seabird, following
168 standard protocol, and quality control parameters. Profiles were bin-averaged at two size
169 intervals: one-meter depth bins and 0.1-meter depth bins, to compare whether bin averaging
170 influenced the heat and salt budgets. We observed no systematic difference between the budget
171 calculations derived from one-meter vs 0.1-meter bins; the results using one-meter bins are
172 presented in this publication. All thermodynamic properties of seawater were evaluated via the
173 Gibbs Seawater toolbox, which uses the International Thermodynamic Equation of Seawater –
174 2010 (TEOS-10). It should be noted that the freezing point calculation can vary slightly,
175 depending on the choice of empirical relationships that are used (e.g. TEOS-10 vs. EOS-80,
176 Nelson et al., 2017).

177

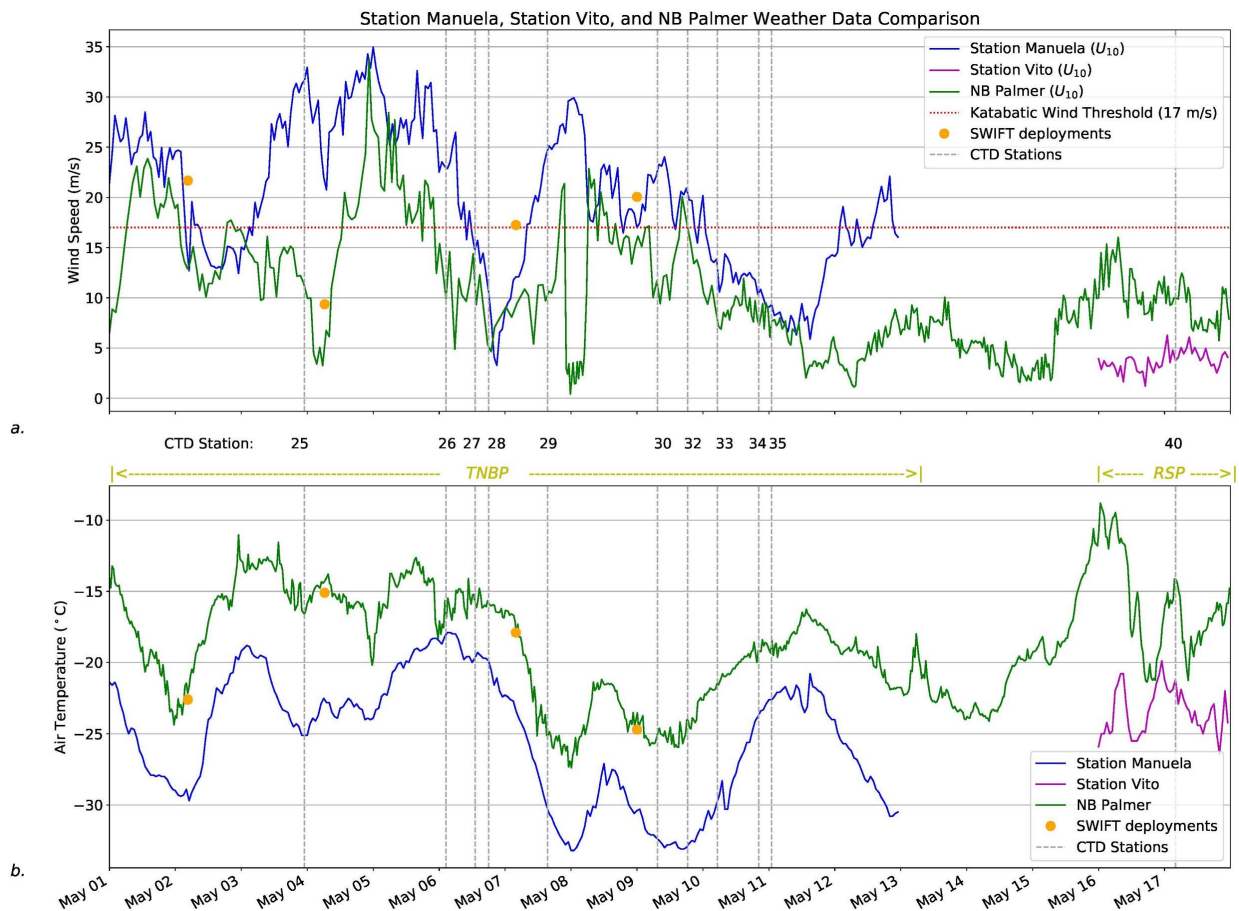
178 **2.4 Weather observations**

179 Weather observations from the NB Palmer meteorological suite during these periods
180 were compared with observations from automatic weather stations Manuela, on Inexpressible
181 Island, and Station Vito, on the Ross Ice Shelf (Figure 2a). Observations from all three were
182 normalized to a height of 10 meters using the logarithmic wind profile (Figure 3). The NB
183 Palmer was in TNB from May 1 through May 13; during this period the hourly wind speed and
184 air temperature data from Weather Station Manuela follow the same pattern, with shipboard
185 observations from the NB Palmer observations being lower in intensity (lower wind speed,
186 warmer temperatures) than Station Manuela. In contrast, the wind speed and air temperature
187 from NB Palmer during its occupation in RSP (May 16-18) is compared to Station Vito. At
188 Station Vito, the air temperature is colder, but the wind speed is less intense. Whereas at Station
189 Manuela (TNBP) the winds are channelized and intensified through adjacent steep mountain

190 valleys, the winds at Station Vito (RSP) are coming off the Ross Ice Shelf, resulting in lower
191 wind speed.

192 During the CTD sampling in the TNBP there were 4 periods of intense katabatic wind
193 events, with each event lasting for at least 24 hours or longer. During the CTD sampling in the
194 RSP there was just one event of near katabatic winds ($> 10 \text{ ms}^{-1}$) lasting about 24 hours. During
195 each wind event, the air temperature oscillated in a similar pattern and ranged from
196 approximately $-10 \text{ }^{\circ}\text{C}$ to $-30 \text{ }^{\circ}\text{C}$.

197



198

199 Figure 3: Weather observations from 01 May to 17 May 2017. a.) Wind speed from Station
200 Manuela (blue line), Station Vito (purple line), NB Palmer (green line), and SWIFT (orange
201 marker) deployments adjusted to 10 meters. The commonly used katabatic threshold of 17 m s^{-1}
202 is depicted as a “dotted red line”, as well as the date and start time of each CTD cast. b) Air
203 temperature from Station Manuela, Station Vito, NB Palmer, and SWIFT deployments.

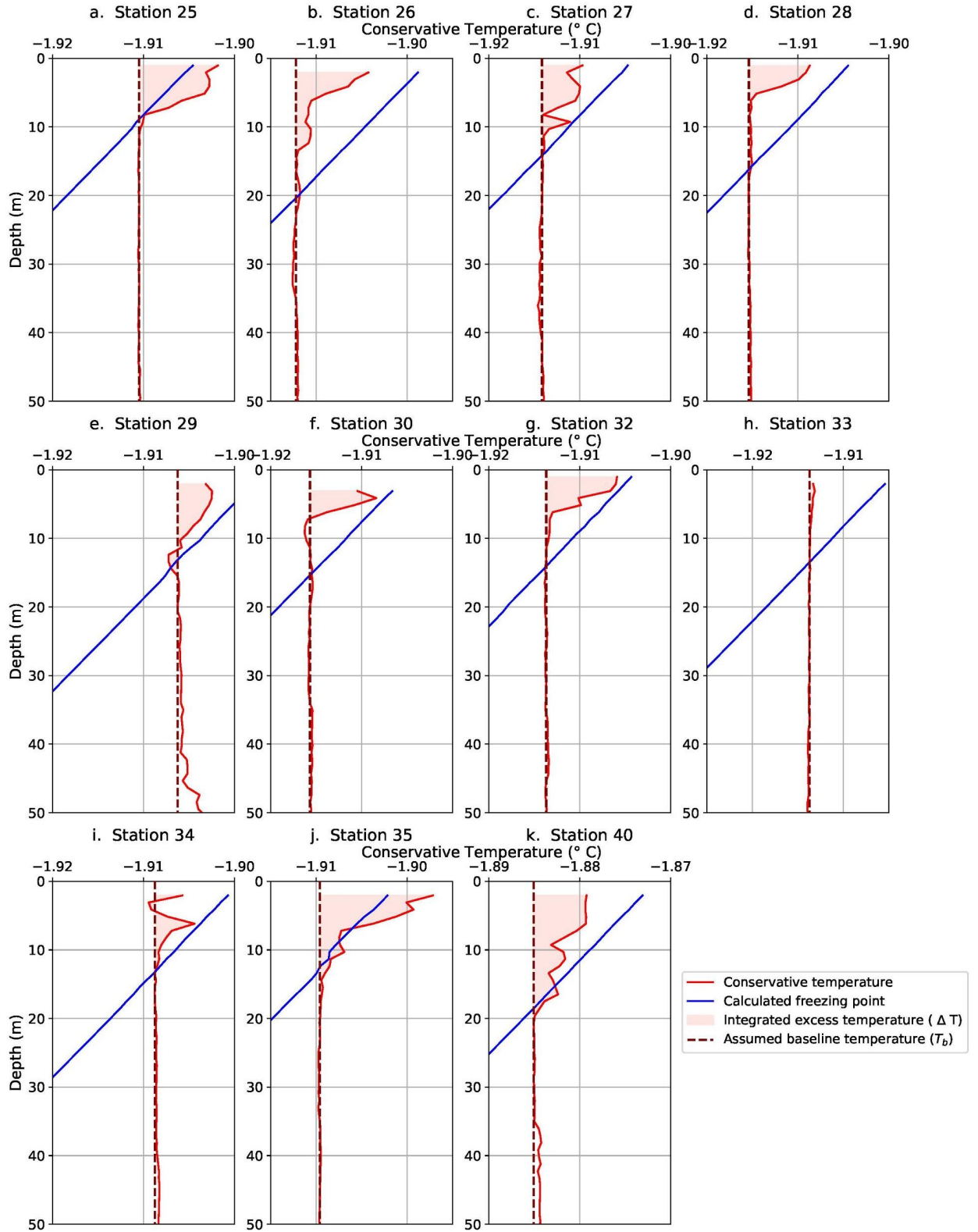
204

205
206
207
208
209
210
211
212
213
214
215
216
217
218
219
220
221
222
223

3. EVIDENCE OF FRAZIL ICE FORMATION

3.1 Selection of profiles

We used the following selection criteria to identify profiles from the two polynyas that appeared to show frazil ice formation: (1) a deep mixed layer extending several hundred meters (Supplemental Figure 2), (2) in-situ temperature readings below the freezing point in the near-surface water (upper five meters), and (3) an anomalous bolus of warm and/or salty water within the top twenty meters of the profile (Figure 4 and 5 plots). For context, all temperature profiles acquired during PIPERS (with the exception of one profile acquired well north of the Ross Sea continental shelf area at 60°S, 170°E) were plotted to show how polynya profiles compared to those outside of polynyas (Supplemental Figure 2).



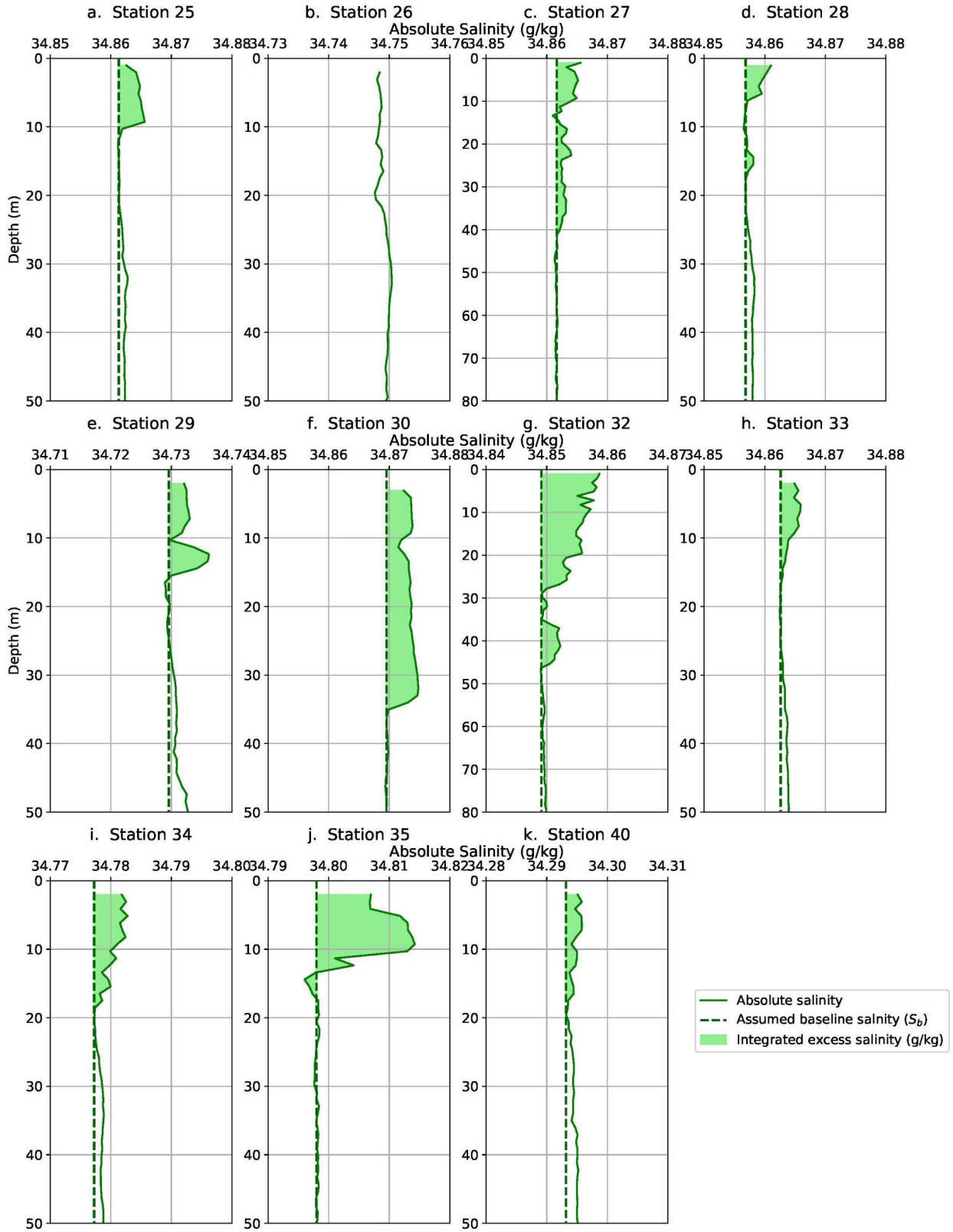
224

225 Figure 4: Conservative Temperature profiles from CTD down casts from 11 stations showing
 226 temperature and/or salinity anomalies. Plots (a-g) and (j-k) all show an anomalous temperature

227 bulge. They also show supercooled water at the surface with the exceptions of (a) and (j). All of
228 the plots (a- k) have an x-axis representing a 0.02 °C change. Profiles (a-j) are from TNBP, and
229 (k) is from RSP.

230 Polynya temperature profiles were then evaluated over the top 50 meters of the water
231 column using criteria 2 and 3. Nine TNBP profiles and one RSP profile exhibited excess
232 temperature anomalies over the top 10-20 m and near-surface temperatures close to the freezing
233 point (Figure 4). Excess salinity anomalies (Figure 5) were observed at the same stations with
234 two exceptions: Station 26 had a measurable temperature anomaly (Figure 4b) but no discernible
235 salinity anomaly (Figure 5b), and Station 33 had a measurable salinity anomaly (Figure 5h) but
236 no discernible temperature anomaly (Figure 4h). The stations of interest are listed in Table 1.

237



239 Figure 5: Absolute Salinity profiles from CTD down casts from 11 stations showing temperature
240 and/or salinity anomalies. Profiles (a) and (c-k) show an anomalous salinity bulge in the top 10-
241 20 meters. Two profiles (c and g) show salinity anomalies extending below 40 meters, so the plot
242 was extended down to 80 meters to best highlight those. All of the plots (a-k) have an absolute
243 salinity range of 0.03 g kg^{-1} .

244

245

246 **3.2 Evaluating the uncertainty in the temperature and salinity anomalies**

247

248 We compared the magnitude of each thermal and haline anomaly to the reported accuracy
249 of the SBE 911 temperature and conductivity sensors: $\pm 0.001 \text{ }^\circ\text{C}$ and $\pm 0.0003 \text{ S m}^{-1}$, or
250 $\pm 0.00170 \text{ g kg}^{-1}$ when converted to absolute salinity. To quantify the magnitude of the
251 temperature anomaly, we computed a baseline excursion, $\Delta T = T_{\text{obs}} - T_{\text{b}}$, throughout the anomaly
252 where T_{obs} is the in-situ conservative temperature and T_{b} is the in-situ baseline, which is
253 extrapolated from the far field conservative temperature within the well-mixed layer below the
254 anomaly (Figure 4). The largest baseline excursion from each of the 11 anomalous CTD profiles,
255 averaged together, yields a value of $\Delta T = 0.0064 \text{ }^\circ\text{C}$. While this is a small absolute change in
256 temperature, it is still 32 times larger than the stated precision of the SBE 911 ($0.0002 \text{ }^\circ\text{C}$). The
257 same approach was applied to the salinity anomalies yielded an average baseline excursion of
258 0.0041 S m^{-1} (or 0.0058 g kg^{-1} for absolute salinity), which is 100 times larger than the
259 instrument precision (0.00004 S m^{-1}). Table 1 lists the maximum temperature and salinity
260 anomalies for each CTD station.

261 The immersion of instruments into supercooled water can lead to a number of unintended
262 outcomes as instrument surfaces may provide ice nucleation sites, or otherwise perturb an
263 unstable equilibrium. Robinson et al., (2020) highlight a number of the potential pitfalls. One
264 concern was that ingested frazil ice crystals could interfere with the conductivity sensor. Crystals
265 smaller than 5 mm can enter the conductivity cell, creating spikes in the raw conductance data.
266 Additionally, frazil crystals smaller than $100 \text{ }\mu\text{m}$ would be small enough to pass between the
267 conductivity electrodes and decrease the resistance/conductance that is reported by the
268 instrument (Skogseth et al, 2009; Robinson et al, 2020). To test for ice crystal interference, the
269 raw (unfiltered with no bin averaging) salinity profile was plotted using raw conductivity

270 compared with the 1-meter binned data for the 11 anomalous CTD Stations (Supplemental
271 Figure 3). The raw data showed varying levels of noise as well as some spikes or excursions to
272 lower levels of conductance; these spikes may have been due to ice crystal interference. Overall,
273 the bin-averaged profile does not appear to be biased or otherwise influenced by the spikes,
274 which tend to fall symmetrically around a baseline. This was demonstrated by bin-averaging
275 over different depth intervals as described in §2.4. It is also worth pointing out that the effect of
276 these conductivity spikes would be to decrease the bin-averaged salinity, thereby working
277 against the overall observation of a positive baseline excursion. In other words, the entrainment
278 of frazil crystals could lead to an underestimate of the positive salinity anomaly, rather than the
279 production of positive salinity aberration.

280 Another pitfall highlighted by Robinson et al., (2020) was the potential for self-heating of
281 the thermistor by residual heat in the instrument housing. The results from their study reveal a
282 thermal inertia that dissipates over a period of minutes. We examined the temperature trace
283 during the CTD soak and did not observe this same behavior. It is possible that some thermal
284 inertia did exist at the time of deployment, but any residual heat appeared to dissipate very
285 quickly, compared to the 3-6 minute soak time before each profile. We suggest the self-heating
286 might be a problem that arose in a single instrument, but is not necessarily diagnostic of all SBE
287 911 models. Those authors did not document this behavior in multiple instruments. Lastly, the
288 potential for ice formation on the surface of the conductivity cell seems unlikely because it was
289 kept warm until it was deployed in the water.

290 The observation of both warm and salty anomalies cannot easily be explained by these
291 documented instrument biases. A cold instrument might be subject to freezing in the
292 conductivity cell, but this would not warm the thermistor that is physically separated from the
293 cell. A warm instrument might have contained residual thermal inertia, which might have melted
294 individual frazil ice crystals, but these would produce negative baseline excursions in salinity,
295 rather than the positive anomaly. The anomalies we observed were found within 11 CTD
296 stations, over the entire length of the polynya, and the same signature could be observed in the
297 up and down cast, although the upcast was slightly smoothed.

298
299
300

301 **3.3 Camera observations of frazil ice formation**

302 During PIPERS an EISCam (Evaluative Imagery Support Camera, version 2) was
303 operating in time lapse mode, recording photos of the ocean surface from the bridge of the ship
304 every 10 minutes (for more information on the EISCam see Weissling et al, 2009). The images
305 from the time in TNBP and RSP reveal long streaks and large aggregations of frazil ice. A
306 selection of photos from TNBP were captured (Figure 6). The winds were strong enough at all
307 times to advect frazil ice, creating downstream frazil streaks, and eventually pancake ice in most
308 situations. Smaller frazil streaks and a curtain of frazil ice below the frazil streak were also
309 visible.
310

a. Photo from 04- May 23:00



c. Photo from 05- May 01:00



b. Photo from 05- May 02:00



d. Photo from 06- May 22:00



311
312 Figure 6: Images from NB Palmer as EISCam (Evaluative Imagery Support Camera) version 2.
313 White areas in the water are loosely consolidated frazil ice crystals being actively formed during
314 a katabatic wind event. Image (d) was brightened to allow for better contrast.

315
316 **3.4 Conditions for frazil ice formation**

317 Laboratory experiments can provide a descriptive picture of the conditions that lead to
318 frazil ice formation; these conditions are diagnostic of conditions in the TNBP. Ushio and
319 Wakatsuchi (1993) exposed a 2 x 0.4 x 0.6 m tank to air temperatures of -10 °C and wind speeds
320 of 6 m s⁻¹. They observed 0.1 to 0.2 °C of supercooling at the water surface and found that after
321 20 minutes the rate of supercooling slowed due to the release of latent heat, coinciding with
322 visually observed frazil ice formation. After ten minutes of ice formation, they observed a
323 measurable increase in temperature of the frazil ice layer of 0.07 °C warmer and 0.5 to 1.0 g kg⁻¹
324 saltier, as a consequence of latent heat and salt release during freezing (Ushio and Wakatsuchi,
325 1993).

326 In this study, we found the frazil ice layer to be on average 0.006 °C warmer than the
327 underlying water. Similarly, the salinity anomaly was on average 0.006 g kg⁻¹ saltier than the
328 water below. While the anomalies we observed were significantly smaller than those observed in
329 the lab tank by Ushio and Wakatsuchi (1993), the trend of super-cooling, followed by frazil ice
330 formation and the appearance of a salinity anomaly is analogous. The difference in magnitude
331 can likely be explained by the reservoir size; the small volume of the lab tank will retain the
332 salinity and temperature anomaly, rather than mixing it to deeper depths.

333 Considering the aggregate of supporting information, we infer that the anomalous profiles
334 from TNBP and RSP were produced by frazil ice formation. The strong winds and sub-zero air
335 temperatures (§2.4), reveal that conditions were sufficient for frazil formation, similar to the
336 conditions observed in the laboratory. We showed that the CTD profiles in both temperature and
337 salinity are reproducible and large enough to be distinguished from the instrument uncertainty
338 (§3.1 and 3.2). Finally, the EISCam imagery reveals the accumulation of frazil ice crystals at the
339 ocean surface.

340

341

342 **4.0 ESTIMATION OF FRAZIL ICE CONCENTRATION USING CTD PROFILES**

343

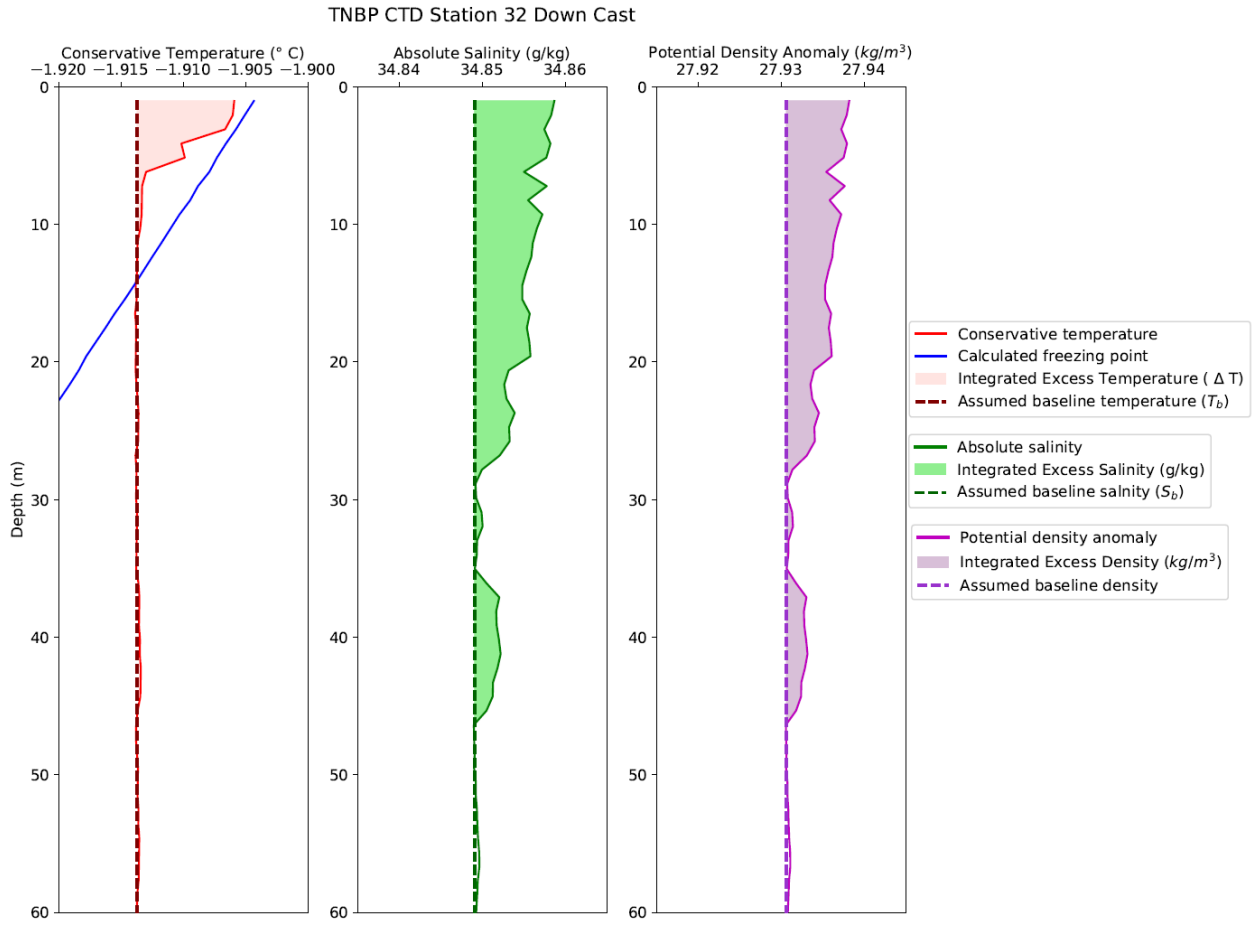
344 Having identified CTD profiles that trace frazil ice formation, we want to know how
345 much frazil ice formation can be inferred from these T and S profiles. The inventories of heat
346 and salt from each profile can provide independent estimates of frazil ice concentration. To
347 simplify the inventory computations, we neglect the horizontal advection of heat and salt; this is

348 akin to assuming that lateral variations are not important because the neighboring water parcels
349 are also experiencing the same intense vertical gradients in heat and salt. We first describe the
350 computation using temperature in § 4.1 and the computation using salinity in § 4.2.

351

352 **4.1 Estimation of frazil ice concentration using temperature anomalies**

353 Using the latent heat of fusion as a proxy for frazil ice production we estimated the
354 amount of frazil ice that must be formed in order to create the observed temperature anomalies.
355 We estimated the excess enthalpy using the same temperature baseline excursion: $\Delta T = T_{\text{obs}} - T_{\text{b}}$,
356 defined in §3.2 . The excess over the baseline is graphically represented in Figure 7a. Because
357 we lacked multiple profiles at the same location, we were not able to observe the time evolution
358 of these anomalies. Consequently, T_{b} represents our best inference of the temperature of the
359 water column prior to the onset of ice formation; it is highlighted in Figure 7a with the dashed
360 line. We established the value of T_{b} by averaging the temperature over a 10 m interval directly
361 beneath the anomaly. In most cases, this interval was nearly isothermal and isohaline, as would
362 be expected within a well-mixed layer. The uncertainty in the value of T_{b} was estimated from
363 the standard deviation within this 10 m interval; the average was $7.5 \times 10^{-5} \text{ }^\circ\text{C}$, which is 1% of
364 the temperature.



366

367 Figure 7: Conservative temperature, absolute salinity, and potential density anomaly for TNBP

368 CTD Station 32, May 9, 2017. a) Conservative temperature profile showing the temperature

369 anomaly, the selected baseline temperature (dashed line) and the integrated excess temperature

370 (shaded area). b) Absolute salinity profile showing the salinity anomaly, the selected baseline

371 salinity (dashed line), and integrated excess salinity (shaded area). c) Potential density anomaly

372 showing the selected baseline density (dashed) and the excess density instability (shaded).

373

374 To find the excess heat (Q_{excess}^{total}) represented in the total thermal anomaly, we computed375 the vertical integral of heat per unit area from the surface ($z=0$) to the bottom of the anomaly376 ($z=z_T$):

$$377 \quad Q_{excess}^{total} = \int_{z=0}^{z=z_T} \rho C_p \Delta T \, dz \quad (1)$$

378 Here ρ is density of seawater, z is the depth range of the anomaly, and C_p is the specific heat
379 capacity, The concentration of frazil ice is estimated by applying the latent heat of formation (L_f
380 = 330 kJ kg⁻¹) as a conversion factor to Q_{excess}^{total} :

$$381 \text{Conc}_{ice}^{temp} = \frac{Q_{excess}^{total}}{L_f \cdot z_T} \quad (2)$$

382 where z_T is the depth of the temperature anomaly in meters. The concentration of ice derived
383 represents the total concentration of ice, in kg m⁻³. A more detailed explanation of equations 1
384 and 2 is contained in Supplemental 1. The mass concentration of ice derived from the
385 temperature anomaly for each station is listed in Table 1.

386

387 **4.2 Estimation of frazil ice concentration using salinity anomalies**

388 The mass of salt within the salinity anomaly was also used to estimate ice formation.
389 Assuming that frazil ice crystals do not retain any brine and assuming there is negligible
390 evaporation, the salinity anomaly is directly proportional to the ice formed. By using the
391 conservation equations for water and salt, the mass of frazil ice can be estimated by comparing
392 the excess salt (measured as salinity) with the amount of salt initially present in the profile,
393 similar to the inventory for heat. The complete derivation can be found in Supplemental 2. The
394 salinity anomaly (ΔS) above the baseline salinity (S_b) is $\Delta S = S_{obs} - S_b$, and is shown in
395 Figure 7b. The initial value of salinity (S_b) was established by observing the trend in the salinity
396 profile directly below the haline bulge; in most cases the salinity trend was nearly linear beneath
397 the bulge, however in general the salinity profiles were less homogeneous than the temperature
398 profiles. We tried to select the starting location as where the anomaly ended and the expected
399 mixed layer traits began. After selecting the starting location from below the anomaly, the
400 absolute salinity was averaged over the next 10 meters to establish a baseline salinity. The
401 uncertainty in the value of S_b was estimated from the standard deviation within this 10 m
402 interval; the average was 2.8×10^{-4} .

403 To find the total mass of frazil ice ($Mass_{ice}^S$, kg m⁻²) in the water column, the integral is
404 taken the salt ratio times the mass of water ($M_W^O = \rho_b dz$, where ρ_b = assumed baseline density=
405 1028 kg m⁻³). The concentration of ice ($Conc_{ice}^{salt}$, kg m⁻³) can be found by dividing the mass of
406 frazil ice by the depth of the salinity anomaly (z_s). The resulting estimates of ice concentration

407 are listed in Table 1.

$$408 \quad Mass_{ice}^S = \rho_b \int_{z=0}^{z=z_S} \frac{\Delta S}{S_{obs}} dz \quad (3)$$

$$409 \quad Conc_{Ice}^{salt} = \frac{Mass_{Ice}^S}{z_S} \quad (4)$$

410 A more detailed explanation of equations 3 and 4 is contained in Supplemental 2 and 3.

411

412 4.3 Summary of the frazil ice estimates

413

414 The derived ice concentrations are listed in Table 1. The salt inventories yielded frazil ice
 415 concentrations from $13 \times 10^{-3} \text{ kg m}^{-3}$ to $266 \times 10^{-3} \text{ kg m}^{-3}$. These estimates were 2 to 9 times
 416 larger than the estimates from the heat inventories. The difference is likely produced by heat loss
 417 to the atmosphere. Sensible and longwave heat exchanges produce an atmospheric loss term in
 418 the heat inventory, which has no corresponding influence on the salt inventory. Therefore, we
 419 suggest that derived ice concentrations from the heat anomalies underestimated frazil ice
 420 concentration in comparison to the salt inventory. We also note the salt inventory has neglected
 421 evaporation. Mathiot et al. (2012) found that evaporation had a small effect on salinity increases,
 422 when compared to ice production and contributed $< 4\%$ to salt flux. In the TNBP, the Palmer
 423 meteorological tower revealed high relative humidity (on average 78.3%), which indicates that
 424 there is likely some evaporation that would reduce the mass of ice derived from the salinity
 425 anomaly by small ($< 4\%$) margin.

426

427 Table 1: CTD Stations with temperature and salinity anomalies (See Figures 4-5), showing
 428 maximum values of the temperature anomaly, depth range of the temperature anomaly,
 429 concentration of ice derived from the temperature anomaly (§4.1), as well as the maximum value
 430 of the salinity anomaly, depth range of salinity anomaly, and concentration of ice derived from
 431 the salinity anomaly (§4.2).

Station	Date and Time	Maximum ΔT ($^{\circ}\text{C}$)	z_T (m)	$Conc_{ice}^{temp}$ (kg m^{-3})	Maximum ΔS (g kg^{-1})	z_S (m)	$Conc_{ice}^S$ (kg m^{-3})

25	May 03 23:00:41	0.009	11.34	48 x 10 ⁻³	0.004	13.4	67 x 10 ⁻³
26*	May 06 02:30:08	0.008	24.73	14 x 10 ⁻³	--	--	--
27	May 06 13:08:11	0.005	15.45	22 x 10 ⁻³	0.003	41.22	46 x 10 ⁻³
28	May 06 17:59:12	0.007	15.52	18 x 10 ⁻³	0.004	17.52	21 x 10 ⁻³
29	May 07 15:29:32	0.004	11.34	22 x 10 ⁻³	0.007	21.64	51 x 10 ⁻³
30	May 09 07:28:24	0.007	8.24	25 x 10 ⁻³	0.005	36.07	105 x 10 ⁻³
32	May 09 18:24:56	0.008	11.33	32 x 10 ⁻³	0.007	47.4	119 x 10 ⁻³
33**	May 10 05:16:29	---	---	---	0.004	22.67	29 x 10 ⁻³
34	May 10 20:16:46	0.004	13.4	9 x 10 ⁻³	0.005	19.58	89 x 10 ⁻³
35	May 11 00:56:32	0.012	19.58	35 x 10 ⁻³	0.016	14.43	266 x 10 ⁻³
40	May 17 04:02:37	0.006	20.61	33 x 10 ⁻³	0.003	18.55	13 x 10 ⁻³

432 *Station 26 did not have a measurable salinity anomaly but was included due to the clarity of the
433 temperature anomaly. Conversely, **Station 33 did not have a measurable temperature anomaly
434 but was included due to the clarity of the salinity anomaly.

435

436 **5.0 ESTIMATION OF TIME SCALE OF ICE PRODUCTION**

437

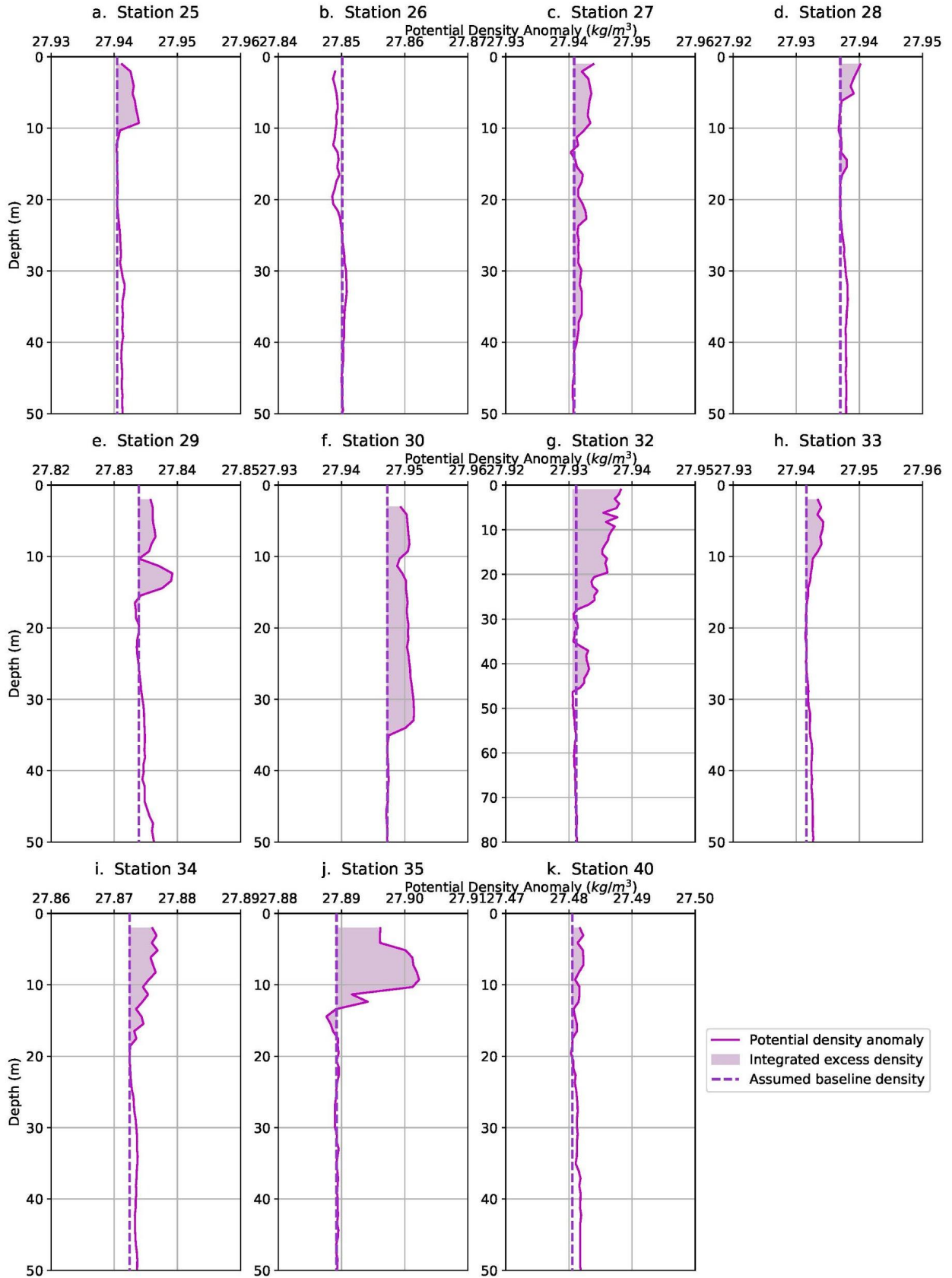
438 How should we interpret the lifetime of these T and S anomalies? Are they short-lived in the
439 absence of forcing, or do they represent an accumulation over some longer ice formation period?

440 One possibility is that the anomalies begin to form at the onset of the katabatic wind event,
441 implying that the time required to accumulate the observed heat and salt anomalies is similar to
442 that of a katabatic wind event (e.g. 12-48 hours). This, in turn would suggest that the estimated
443 frazil ice production took place over the lifetime of the katabatic wind event. Another
444 interpretation is that the observed anomalies reflect the near-instantaneous production of frazil
445 ice. In this scenario, heat and salt are simultaneously produced and actively mixed away into the
446 far field. In this case, the observed temperature and salinity anomalies reflect the net difference
447 between production and mixing. One way to address the question of lifetime is to ask “if ice
448 production stopped, how long would it take for the heat and salt anomalies to dissipate?” The
449 answer depends on how vigorously the water column is mixing. In this section, we examine the
450 mixing rate. However, we can first get some indication of the timescale by the density profiles.

451

452 **5.1 Apparent instabilities in the density profiles**

453 The computed density profiles reveal an unstable water column for all but one of our
454 eleven stations (Figure 8). These suggest that buoyancy production from excess heat did not
455 effectively offset the buoyancy loss from excess salt within each anomaly. It is not common to
456 directly observe water column instability without the aid of microstructure or other instruments
457 designed for measuring turbulence.



459 *Figure 8: Potential density anomalies for all 11 stations with evidence of active frazil ice*
460 *formation. The integrated excess density and assumed baseline density are depicted to highlight*
461 *the instability. Note that Station 26 (b) does not present a density anomaly because it does not*
462 *have a salinity anomaly. In the absence of excess salinity, the temperature anomaly created*
463 *instead an area of less dense water (i.e., a stable anomaly).*

464

465 We suggest that an instability in the water column that persists long enough to be
466 measured in a CTD profile, must be the result of a continuous buoyancy loss that is created at a
467 rate faster than it can be eroded by mixing. In other words, the katabatic winds appeared to
468 dynamically maintain these unstable profiles. Continuous ice production leads to the production
469 of observed heat and salt excesses at a rate that exceeds the mixing rate. If the unstable profiles
470 reflect a process of continuous ice production, then the inventory of ice that we infer from our
471 simple heat and salt budgets must reflect ice production during a relatively short period of time,
472 defined by the time it would take to mix the anomalies away, once the wind-driven dynamics and
473 ice production stopped.

474 Similarly, Robinson et al (2014) found that brine rejection from platelet ice formation
475 also leads to dense water formation and a static instability. Frazil ice formation from continually
476 supplied Ice Shelf Water, formed from ice shelf melt and subject to pressure-induced
477 supercooling, created a stationary instability, which was observable before being mixed by
478 convection to the underlying homogeneous water column that extended to 200 meters (Robinson
479 et al, 2014).

480

481 **5.2 Lifetime of the salinity anomalies**

482

483 To estimate the lifetime of each salinity anomaly requires an estimate of the rate of
484 turbulent mixing in the mixed layer. The Kolmogorov theory for turbulent energy distribution
485 defines the eddy turnover time as the time it takes for a parcel to move a certain distance, d , in a
486 turbulent flow (Valis, 2017). The smallest eddy scale is that of turbulent energy dissipation, and
487 the largest scale is bounded by the length of the domain and the free stream turbulent velocity
488 (Cushman-Roisin, 2019). This timescale can be estimated as,

489
$$t \approx \frac{d}{(\varepsilon d)^{\frac{1}{3}}} \approx \left(\frac{d^2}{\varepsilon}\right)^{\frac{1}{3}} \quad (5)$$

490 Here, d is the characteristic length of the largest eddy and ε is the turbulent kinetic energy (TKE)
 491 dissipation rate, which is related to the free stream velocity as $\varepsilon \sim w^3/d$ (Cushman-Roisin, 2019).
 492 In this section we discuss and derive the best available estimates t using measurements of the
 493 meteorological forcing conditions and in-situ measurements of the turbulence.

494 If d is bounded only by the domain (in this case, the mixed layer depth), this would
 495 suggest vertical turbulent eddies up to 600 m in length (Table 2). However, a homogenous
 496 mixed-layer does not necessarily imply active mixing throughout the layer (Lombardo and
 497 Gregg, 1989). Instead, the length scale of the domain is more appropriately estimated from the
 498 size of the buoyancy instability and the background wind shear, or the Monin-Obukhov length
 499 (L_{M-O}) (Monin & Obukhov, 1954). When L_{M-O} is small and positive, buoyant forces are
 500 dominant and when L_{M-O} is large and positive, wind shear forces are dominant (Lombardo &
 501 Gregg, 1989). The L_{M-O} can be expressed the salt-driven buoyancy flux, reflecting the same
 502 process that gave rise to the observed salinity anomalies (see §4.3 for more detail).

503
 504
$$L_{M-O} = -\frac{u_*^3}{k\beta gw\overline{\Delta S}} \quad (6)$$

505
 506 where u_* is the aqueous friction velocity, g is gravitational acceleration, w is the water vertical
 507 velocity, $\overline{\Delta S}$ is the salt flux, β is the coefficient of haline contraction, and k is the von Karman
 508 constant. A more detailed explanation, along with the specific values are listed in Supplemental
 509 4.

510 The friction velocity derives from the wind speed (U_{palmer}), measured at the NB Palmer
 511 weather mast from a height of $z_{palmer} = 24$ m, adjusted to a 10 meter reference (U_{10}) (Manwell
 512 et al., 2010).

513
 514
$$U_{10} = U_{palmer} \frac{\ln\left(\frac{z}{z_0}\right)}{\ln\left(\frac{z_{palmer}}{z_0}\right)} \quad (7)$$

515
 516 Roughness class 0 was used in the calculation and has a roughness length of 0.0002 m. These
 517 values are used to estimate the wind stress as,

$$518 \quad \tau = C_D \rho_{air} U_{10}^2 \quad (8)$$

519 where ρ_{air} represents the density of air, with a value of 1.3 kg m^{-3} calculated using averages
 520 from NB Palmer air temperature ($-18.7 \text{ }^\circ\text{C}$), air pressure (979.4 mbars) and relative humidity
 521 (78.3%). C_D , the dimensionless drag coefficient, was calculated as 1.525×10^{-3} using the
 522 NOAA COARE 3 model, modified to incorporate wave height and speed (Fairall et al, 2003).
 523 The average weather data from NB Palmer was paired with the wave height and wave period
 524 from the SWIFT deployment (defined below) on 04 May to find C_D . A more detailed explanation
 525 and the specific values are listed in Supplemental 5. Finally, u_* from equation (6) is:

$$526 \quad u_* = \sqrt{\frac{\tau}{\rho_{water}}} \quad (9)$$

527
 528 During the katabatic wind events, a SWIFT (Surface Wave Instrument Float with
 529 Tracking) buoy was deployed to measure TKE dissipation and vertical velocity, w , and wave
 530 field properties. (Thomson, 2012; Thomson et al, 2016; Zippel & Thomson, 2016). SWIFT
 531 deployments occurred within the period of CTD observations, as shown in the timeline of events
 532 (Supplemental Figure 5), however they do not coincide in time and space with the CTD profiles.
 533 For the vertical velocity estimation, we identified the May 04 and May 09 SWIFT deployments
 534 as most coincident to CTD stations analyzed here, based on similarity in wind speeds. The
 535 average wind speed at all the CTD stations with anomalies was 10.2 m s^{-1} . For the May 4 SWIFT
 536 deployment, the wind speed was 9.36 m s^{-1} . CTD Station 32 experienced the most intense
 537 sustained winds of 18.9 m s^{-1} . The May 9 SWIFT deployment was applied to CTD 32, which had
 538 a wind speed of 20.05 m s^{-1} . During these SWIFT deployments, the average vertical velocity (w)
 539 was measured in the upper meter of the column. May 04 had an average value of $w= 0.015 \text{ m s}^{-1}$
 540 and May 09 had an average value of $w= 0.025 \text{ m s}^{-1}$. See Thomson (2012), Thomson et al.,
 541 (2016) & Zippel & Thomson, (2016) for details on how these measurements are made.

542 The TKE dissipation rates are expected to vary with wind speed, wave height, ice
 543 thickness and concentration (Smith & Thomson, 2019). Wind stress is the source of momentum
 544 to the upper ocean, but this is modulated by scaling parameter (c_e , Smith & Thomson, 2019). If
 545 the input of TKE is in balance with the TKE dissipation rate over an active turbulent layer, the
 546 following expression can be applied:

$$547 \quad c_e \tau \propto \rho \int \varepsilon(z) dz \quad (10)$$

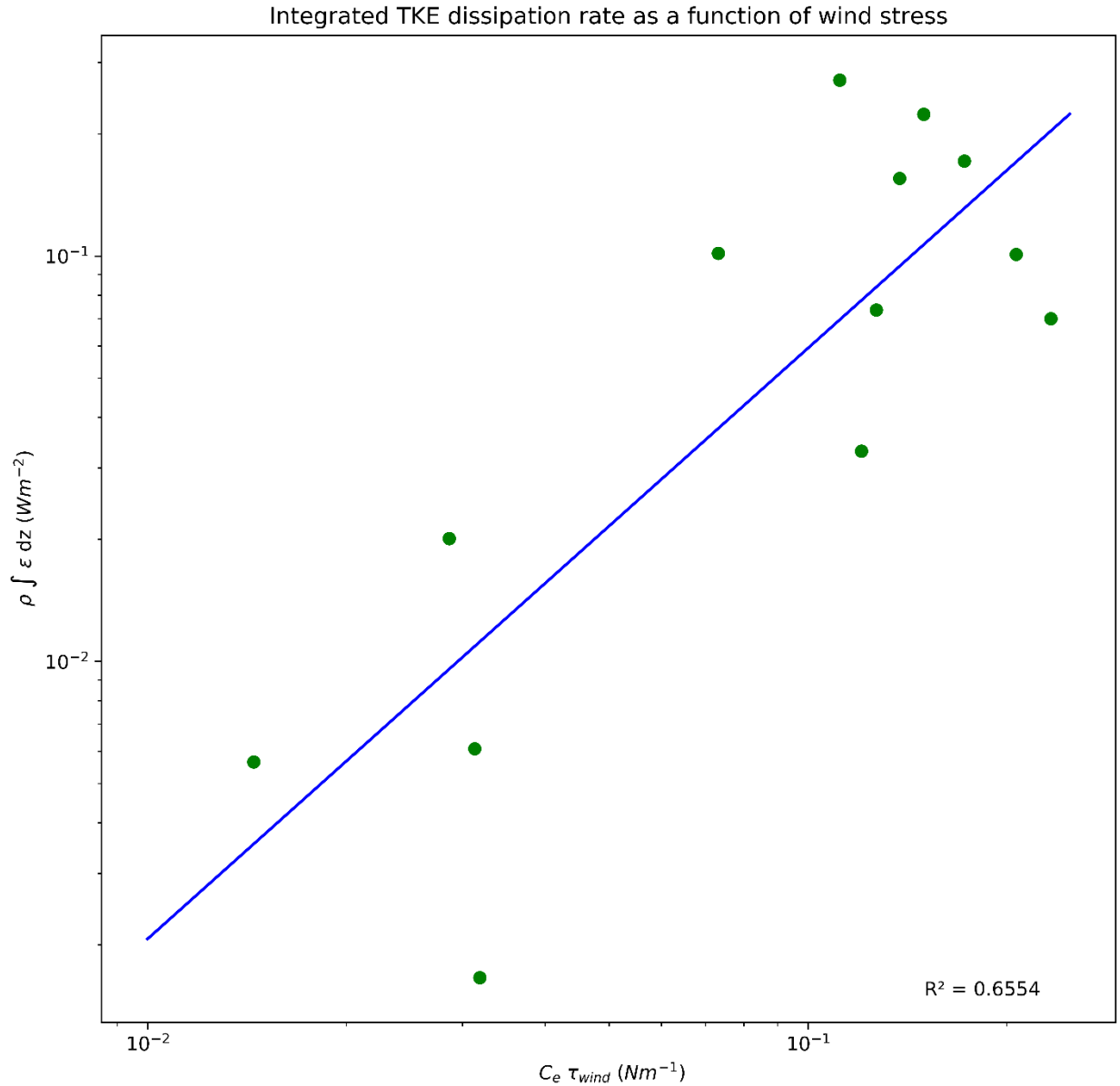
548

549 where the density of water (ρ) is assumed to be 1027 kg m^{-3} for all stations. This scaling
550 parameter incorporates both wave and ice conditions; more ice produces more efficient wind
551 energy transfer, while simultaneously damping surface waves, with the effective transfer velocity
552 in ice, based on the assumption that local wind input and dissipation are balanced Smith &
553 Thompson (2019) used the following empirical determination of c_e :

$$554 \quad c_e = a \left(A \frac{z_{ice}}{H_s} \right)^b \quad (11)$$

555 Here, A is the fractional ice cover, with a maximum value of 1, z_{ice} is the thickness of ice, and H_s
556 is the significant wave height. Using Antarctic Sea ice Processes and Climate or ASPeCt visual
557 ice observations (www.aspect.aq) from NB Palmer, the fractional ice cover and thickness of ice
558 were found at the hour closest to both SWIFT deployments and CTD profiles (Knuth & Ackley,
559 2006; Ozsoy-Cicek et al., 2009; Worby et al., 2008). SWIFT wave height measurements yielded
560 an average value of $H_s = 0.58 \text{ m}$ for May 04, and this value was applied to all the CTD profiles.
561 To obtain the most robust data set possible, in total, 13 vertical SWIFT profiles from May 2,
562 May 4, and May 9 were used to evaluate equation 12 over an active depth range of 0.62 meters.

563 Using the estimates of c_e , τ , and ϵ from the SWIFT, we parameterized the relationship
564 between wind stress and ϵ that is reflected in equation (10). A linear fit on a log-log scale ($y =$
565 $10^{(1.4572 \log_{10}(x) + 0.2299)}$, $r^2 = 0.6554$) was then applied to NB Palmer wind stress data to derive
566 turbulent kinetic dissipation estimates that coincided with the ambient wind conditions during
567 each CTD station (Table 2).



568

569 Figure 9: Input wind-driven TKE into the surface ocean versus the TKE dissipation rate over the
 570 active depth range. A linear scaling relationship was applied to the log of each property.

571

572 Gathering these estimates of w , u^* , and ϵ , we have the necessary elements to estimate the
 573 anomaly lifetime using equation (5). Because L_{M-O} has been chosen to represent the domain
 574 length scale, we rewrite equation (5) as:

575
$$t = \left(\frac{L_{M-O}^2}{\epsilon} \right)^{\frac{1}{3}} \quad (12)$$

576

577 Haline contraction, β , in equation (6) was calculated from Gibbs Seawater toolbox and
578 averaged over the depth range of the anomaly. The excess salt, $\overline{\Delta S}$, was found using the average
579 value of ΔS for each profile anomaly. The values of L_{M-O} range from 6 m to 330 m (Table 2). In
580 general, L_{M-O} was greater than the length of the salinity anomaly but smaller than the mixed
581 layer depth.

582 The mixing lifetime of these salinity anomalies ranged from 2 to 12 minutes, but most
583 values cluster near the average of 9 min. The average timescale is similar to the frazil ice lifetime
584 found in Michel (1967). **These lifetimes suggest that frazil ice production and the observed**
585 **density instabilities relax to a neutral profile within ten minutes of a diminution in wind**
586 **forcing.**

587

588 6.0 RATE OF FRAZIL ICE PRODUCTION

589 We can extend the analysis of anomaly lifetime to estimate the frazil ice production rate.
590 Heuristically, the lifetime of the anomaly is equivalent to the time it would take for the anomaly
591 to be dissipated, or *produced*, given the observed conditions of heat loss to the atmosphere. By
592 that analogy, the sea ice production rate is,

593

$$594 \text{ Production rate} = \frac{\text{Conc}_{ice}^{salt} z_S}{t \rho_{ice}} \quad (13)$$

595 Here, $\rho_{ice} = 920 \text{ kg m}^{-3}$, and z_S = the depth of the salinity anomaly (m). The results are
596 summarized in Table 2. A more detailed explanation and the individual terms from equation 13
597 are listed in Supplemental 6. To capture the uncertainty in the sea ice production rates, we used
598 the Student t-distribution to derive confidence intervals (CI) for TKE dissipation rate at each
599 CTD station was used to bound the range of ice production rates, which are reported in Table 2.
600 Uncertainty in the heat and salt inventories were not included in the uncertainty estimates,
601 because we observed negligible difference in the inventory while testing the inventory for effects
602 associated with bin averaging of the CTD profiles (Section 2.3). Another small source of error
603 arises from the neglect of evaporation. To quantify the amount of error introduced by that
604 assumption, we used the bulk aerodynamic formula for latent heat flux and found the effects of
605 evaporation across the CTD stations to be 1.8% [0.07-3.45%] (Zhang, 1997). This error due to
606 the effects of evaporation found are similar to Mathiot et al (2012). On average, the lower limit

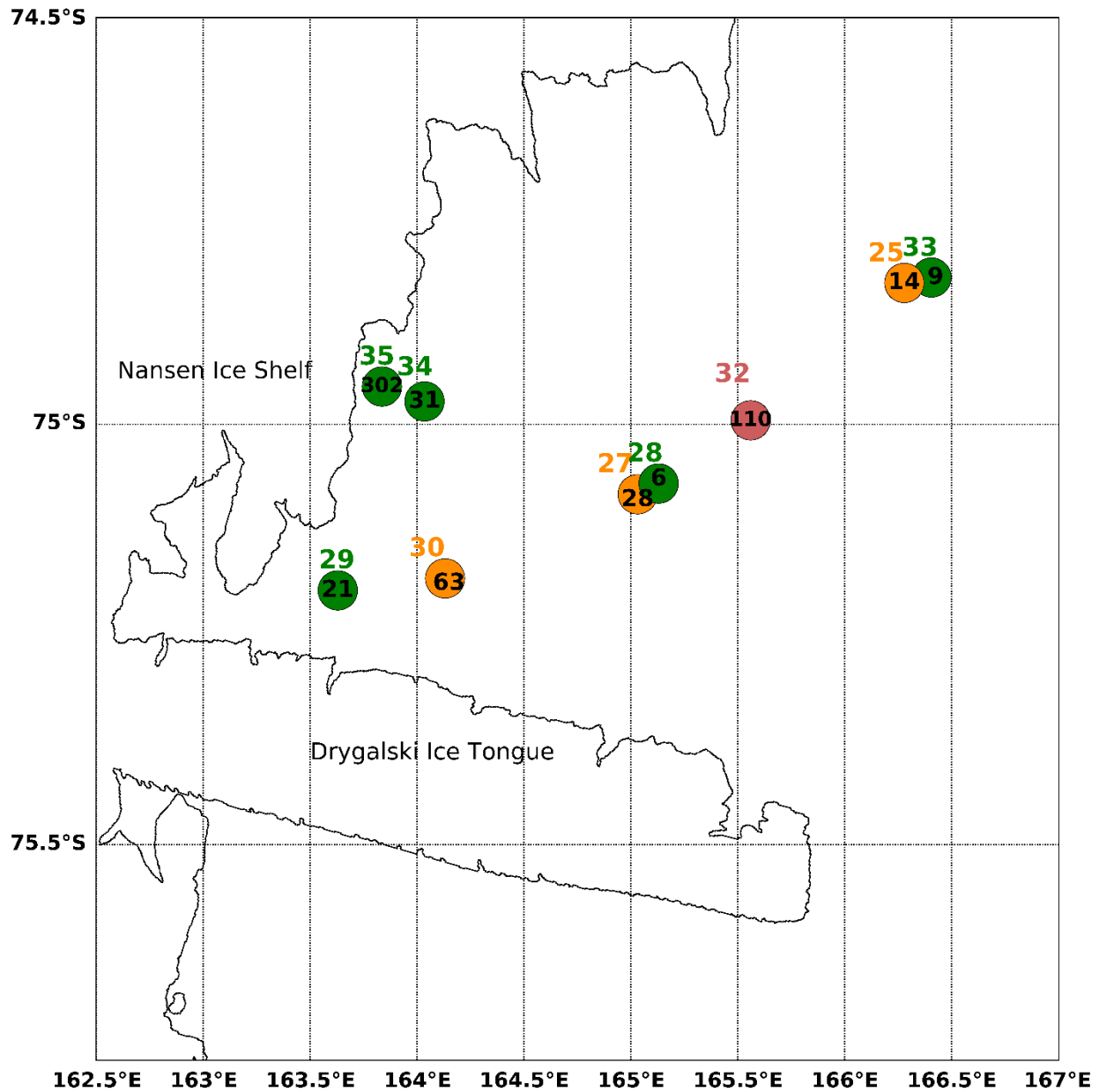
607 of ice production was 30% below the estimate and the upper limit was some 44% larger than the
608 estimated production.

609 The estimates of frazil ice production rate span two orders of magnitude, from 3 to 302
610 cm d^{-1} , with a median ice production is 28 cm d^{-1} . The highest ice production estimate occurred
611 at CTD 35, closest to the Antarctic coastline and the Nansen Ice Shelf. The next largest value is
612 110 cm d^{-1} , suggesting the ice production at CTD 35 is an outlier, and may be a consequence of
613 platelet ice in upwelling ice shelf water (Robinson et al., 2014). Here forward, we will exclude
614 the ice production rate at CTD 35 from the trend analysis.

615 The remaining ice production rates, span a range from 3 to 110 cm d^{-1} and reveal some
616 spatial and temporal trends that correspond with the varying conditions in different sectors of the
617 TNBP. A longitudinal gradient emerges along the length of the polynya, when observing a
618 subset of stations, categorized by similar wind conditions CTD 30 ($U_{10}=11.50 \text{ m s}^{-1}$), CTD 27
619 ($U_{10}=10.68 \text{ m s}^{-1}$), and CTD 25 ($U_{10}=11.77 \text{ m s}^{-1}$). Beginning upstream near the Nansen Ice
620 shelf (Station 30) and moving downstream along the predominant wind direction toward the
621 northeast, the ice production rate decreases. The upstream production rate is 63 cm day^{-1}
622 followed by midstream values of 28 cm day^{-1} , and lastly downstream values of 14 cm day^{-1} .

623 The spatial trend we observed somewhat mimics the 3D model of TNBP from Gallee
624 (1997). During a four-day simulation, Gallee found highest ice production rates near the coast
625 (e.g. our Station 35) of 50 cm day^{-1} , and decreased to 0 cm day^{-1} downstream and at the outer
626 boundaries, further west than PIPERS Station 33 (Figure 10). While some of the ice production
627 rates derived from PIPERS CTD profiles exceed prior results, we attribute that excess to the
628 relatively short time scale of these ice production “snapshots”. These estimates integrate over
629 minutes to tens of minutes, instead of days to months, therefore they are more likely to capture
630 the high frequency variability in this ephemeral process. As the katabatic winds oscillate, the
631 polynyas enter periods of slower ice production, driving average rates down.

632



634

635 Figure 10: TNBP map of ice production rates. Map of TNBP CTD stations with anomalies and
 636 ice production rates. The CTD station number is listed in to the north of the stations. Listed
 637 inside the circle in black is the respective ice production rate in cm day^{-1} . The symbols and
 638 station numbers are colored by wind speed: Green indicates wind speeds less than 10 m s^{-1}
 639 (Stations 28, 29, 33, 34, 35), Orange indicates wind speeds between 10 and 15 m s^{-1} (Stations 25,
 640 27, 30), and Red indicated wind speeds over 15 m s^{-1} (Station 32).

641

642

643 Table 2: Summary of mass of ice derived from salinity, lifetime, and production rates.

Station	$Conc_{ice}^S$ (kgm^{-3})	z_s (m)	L_{M-o} (m)	TKE diss. ε ($\text{m}^2 \text{s}^{-3}$)	MLD (m)	Timescal e/ Lifetime (t) (min)	Production rate (cm day^{-1})	Production rate 95% CI (cm day^{-1})
25	67×10^{-3}	13.4	141	9.648×10^{-5}	350	9.8	14	[10 - 20]
26*	--	--	--	7.191×10^{-5}	100	---	---	--
27	46×10^{-3}	41.2	151	8.188×10^{-5}	500	10.9	28	[20- 37]
28	21×10^{-3}	17.5	54	1.622×10^{-5}	600	9.4	6	[4- 10]
29	51×10^{-3}	21.6	80	5.375×10^{-5}	275	8.2	21	[15 - 28]
30	105×10^{-3}	36	83	3.771×10^{-5}	500	9.5	63	[45- 88]
32	119×10^{-3}	47	198	3.466×10^{-4}	375	8.0	110	[67-181]
33	29×10^{-3}	23.7	98	2.844×10^{-5}	500	11.6	9	[5- 13]
34	89×10^{-3}	19.6	66	6.397×10^{-5}	175	6.8	31	[23 - 42]
35	266×10^{-3}	14.4	6	2.343×10^{-5}	150	2.0	302	[200- 456]

	10 ⁻³			10 ⁻⁵				
40	13 x 10 ⁻³	18.6	175	9.603 x 10 ⁻⁵	120	11.7	3	[2- 5]

644 *Station 26 did not have a measurable salinity anomaly but was included due to the clarity of the
645 temperature anomaly. The term MLD stands for estimated mixed layer depth.

646

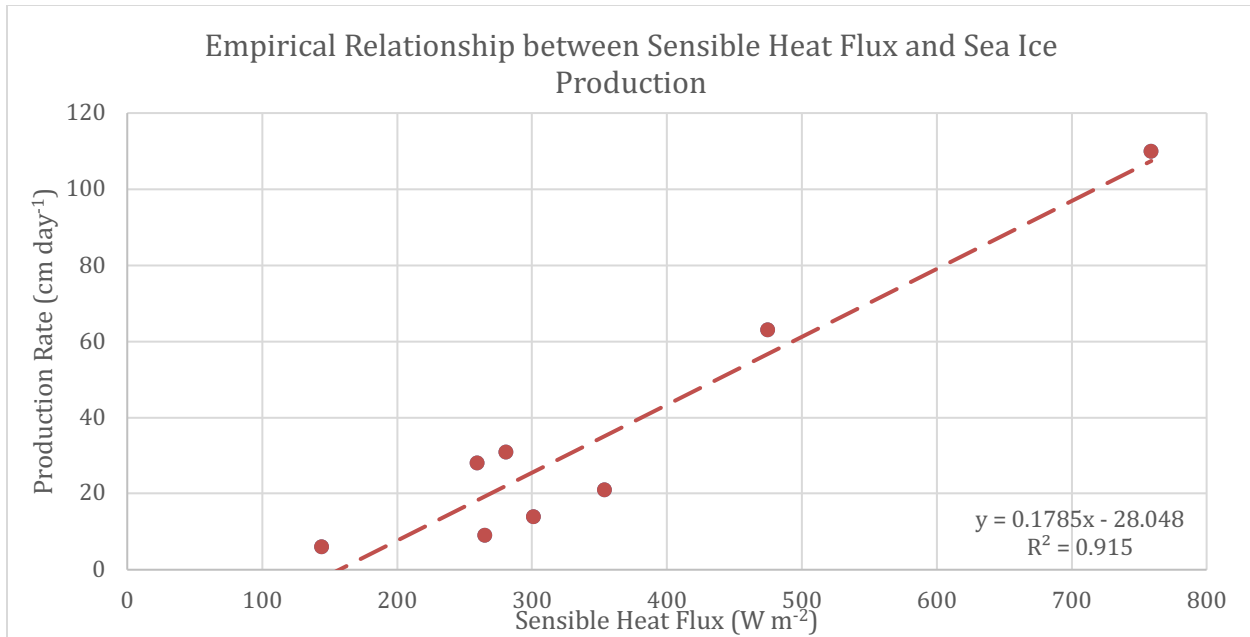
647 6.1 Seasonal Ice Production

648 We can estimate the seasonal average in sea ice production by relating these in-situ ice
649 production estimates to the atmospheric forcing. The sensible heat flux (Q_s), measured at the
650 automated weather station Manuela, was used to empirically scale the ice production rates for the
651 season.

$$652 \quad Q_s = c_p \rho_a C_s u_{10} (T_b - T_a) \quad (14)$$

653 here $c_p = 1.003 \text{ kJ kg}^{-1} \text{ K}^{-1}$, the specific heat capacity of air at $-23 \text{ }^\circ\text{C}$, $C_s = 1.297 \times 10^{-3}$, is the
654 heat transfer coefficient calculated using the COARE 3.0 code (Fairall et al, 2003). The values
655 are included in Supplemental Table S6.

656 The sensible heat flux was calculated using NB Palmer meteorological data, from times
657 coinciding with the TNBP CTD stations. Station 35 (see §5.1) and Station 40, in the Ross Sea
658 Polynya, were excluded from this calculation. Figure 11 depicts the trend between Q_s and sea ice
659 production rate; the high degree of correlation ($R^2 = 0.915$) likely occurs because the same NB
660 Palmer wind speeds were used in the calculation of both Q_s and sea ice production (equation 7);
661 in other words, the two terms are not strictly independent of each other.



662
 663 Figure 11: Empirical relationship between sensible heat flux and sea ice production: Production
 664 rate = $0.1785 Q_s - 28.048$, R^2 of 0.915.
 665

666 The met data from the NB Palmer and from Station Manuela (Figure 3) reveal that TNBP
 667 experiences slower wind speeds and warmer temperatures than Station Manuela. This
 668 phenomenon has been explained as a consequence of adiabatic warming and a reduction in the
 669 topographic ‘Bernoulli’ effects that cause wind speed to increase at Station Manuela (Schick,
 670 2018). Before applying the time series of met data from Manuela to equation 14 to calculate Q_s ,
 671 we needed to account for the offset. On average, the air temperatures were 6.5 °C warmer, and
 672 wind speed was on 7.5 $m s^{-1}$ slower in TNB, during the 13 days that the vessel was in the
 673 polynya. Figure S6 shows the corrected data against the original data for the time in TNB.

674 We estimated the seasonal average in Q_s over TNBP using the corrected met data from
 675 Station Manuela, and an average sea surface temperature from the CTD stations (-1.91 °C), the
 676 air density, specific heat capacity, and heat transfer coefficient remained the same as above.
 677 The average in Q_s from April to September is 321 $W m^{-2}$. Using the empirical relationship
 678 described in Figure 11, the seasonal average of frazil ice production in Terra Nova Bay polynya
 679 is 29 $cm day^{-1}$.

680 The seasonal sea ice production rate varies based on many factors affecting the rate of
 681 heat loss from the surface ocean. These factors include a strong negative feedback between
 682 ocean heat loss and sea ice cover. As the polynya builds up with ice, heat fluxes to the
 683 atmosphere will decline (Ackley et al, 2020 in review) until that ice cover is swept out of the

684 polynya by the next katabatic wind event. This spatial variation in ice cover and wind speed,
685 produces strong spatial gradients in the heat loss to the atmosphere that drives ice production.
686 For example, Ackley et al., (Figure 3, 2020 in review) observed heat flux variations from nearly
687 2000 W m^{-2} to less than 100 W m^{-2} over less than 1 km. An integrated estimate of total polynya
688 sea ice production should take these spatial gradients and the changes in polynya area into
689 account. That analysis is somewhat beyond the scope of this study, but we anticipate including
690 these ice production estimates within forthcoming sea ice production estimates for 2017 and
691 PIPERS.

692 One interesting outcome of the scaling relationship in Figure 11, is the value of the y-
693 intercept at 157 W m^{-2} . This relationship suggests that frazil ice production ceases when the heat
694 flux falls below this range. This lower bound, in combination with the spatial gradients in heat
695 flux may help to establish the region where active production is occurring.

696

697 **6.2 Comparison to prior model and field estimates of ice production**

698 The 29 cm d^{-1} of seasonal average ice production that we estimated here, falls within the
699 range of other in-situ ice production estimates. Schick (2018) estimated a seasonal average ice
700 production rate of 15 cm day^{-1} , and Kurtz and Bromwich (1985), determined 30 cm day^{-1} . Both
701 studies derived their ice production rates using a heat budget.

702 Overall, these ice production estimates from in-situ data are larger than the seasonal
703 production estimates derived from remote sensing products. Drucker et al (2011) used the
704 AMSR-E instrument to obtain a seasonal average of 12 cm day^{-1} for years 2003-2008. Oshima et
705 al, (2016) estimated 6 cm day^{-1} of seasonal production for the years 2003-2011, and Nihashi and
706 Ohshima (2015) determined 7 cm day^{-1} for years 2003-2010. Finally, Tamura et al (2016) found
707 production rates that ranged from $7\text{-}13 \text{ cm day}^{-1}$, using both ECMWF and NCEP Reanalysis
708 products for 1992-2013, reflecting a greater degree of consistency in successive estimates, likely
709 because of consistency in the estimation methods.

710 Using a sea ice model, Sansiviero et al (2017) estimated seasonal average production of
711 27 cm day^{-1} . Petrelli et al (2008) modeled an average daily rate of production of 14.8 cm day^{-1} in
712 the active polynya, using a coupled atmospheric-sea ice model. Fusco et al (2002) applied a
713 model for latent heat polynyas and estimated a seasonal average production rate of 34 cm day^{-1}
714 for 1993 and 29 cm day^{-1} for 1994, which is comparable to the in-situ budgets.

715
716
717
718
719
720
721
722
723
724
725
726
727
728
729
730
731
732
733
734
735
736
737
738
739
740
741
742
743
744
745

7. CONCLUSIONS

Polynyas have been regarded as ice production factories, which are responsible for total volumetric ice production that is vastly disproportionate to their surface area. This study has documented temperature and salinity anomalies in the upper ocean that reflect vigorous frazil ice production. These anomalies produce an unstable water column that can be observed as a quasi-stationary feature in the density profile. The only comparable example is found in the outflow of supercooled ice shelf waters. These features were observed during strong katabatic wind events in the Terra Nova Bay and the Ross Sea polynyas, with heat losses in excess of 2000 W m^{-2} . The anomalies provide additional insights into the ice production within polynyas, and have provided estimates of frazil ice production rates, in-situ. The frazil production rates varies from 3 to 110 cm day^{-1} , with a seasonal average of 29 cm day^{-1} , and the method captures ice production on very on the timescale of minutes to tens of minutes, which is significantly shorter than the more common daily or monthly production rates. It is not clear how many frazil ice crystals survive to become part of the consolidated seasonal ice pack. In this vigorous mixing environment, a significant fraction may melt and become reincorporated into the ocean, before they have a chance to aggregate.

By the same token, frazil production and the estimates of ice production could be improved by collecting consecutive CTD casts at the same location, to observe how these anomalies evolve on the minute-to-minute timescale. This is a challenging environment and recent studies have documented the fate of instruments during long-term exposure to frazil ice slurries. However, one exciting outcome of this study is the suggestion that it is possible to obtain synoptic inventories of ice production. For example, a float or glider that measures surface CTD profiles on a frequent basis, would improve our synoptic and seasonal understanding of polynya ice production as they respond to annual and secular modes of the ocean and atmosphere.

746
747
748
749
750
751
752
753
754
755
756
757
758
759
760
761
762
763
764
765
766
767
768
769
770
771
772
773
774
775
776

8. REFERENCES

- Ackley, S.F., Stammerjohn, S., Maksym, T. Smith, M., Cassano, J., Guest P. Tison, J-L., Delille, B. Loose, B., Sedwick, P. DePace, L., Roach, L., Parno, J. Sea ice production and air-ice-ocean-biogeochemistry interactions in the Ross Sea during the PIPERS 2017 autumn field campaign, *Ann. Glaciol.*, 2020 in review.
- Armstrong, T.: World meteorological organization: wmo sea-ice nomenclature. terminology, codes and illustrated glossary, *J. Glaciol.*, 11, 148-149, <https://doi.org/10.3189/S0022143000022577>, 1972.
- Bromwich, D. H., and Kurtz, D. D.: Katabatic wind forcing of the terra nova bay polynya, *J. Geophys. Res.*, 89, 3561-3572, <https://doi.org/10.1029/JC089iC03p03561>, 1984.
- Buffoni, G., Cappelletti, A., and Picco, P.: An investigation of thermohaline circulation in terra nova bay polynya, *Antarct. Sci*, 14.1, 83-92, <https://doi.org/10.1017/S0954102002000615>, 2002.
- Cosimo J.C., and Gordon A.L.: Inter-annual variability in summer sea ice minimum, coastal polynyas and bottom water formation in the weddell sea, in: *Antarctic sea ice: physical processes, interactions and variability*, 74, edited by: Jeffries, M.O., American Geophysical Union, Washington, D.C., 293-315, <https://doi.org/10.1029/AR074p0293>, 1998.
- Cox, G. F. N., and Weeks, W. F.: Equations for determining the gas and brine volumes in sea-ice samples, *J. Glaciol.*, 29, 306-316, <https://doi.org/10.3189/S0022143000008364>, 1983.
- Cushman-Roisin, B.: *Environmental Fluid Mechanics*, John Wiley & Sons, New York, 2019.

777 Dmitrenko, I. A., Wegner, C., Kassens, H., Kirillov, S. A., Krumpfen, T., Heinemann, G.,
778 Helbig, A., Schroder, D., Holemann, J.A., Klagger, T., Tyshko, K.P., and Busche, T.:
779 Observations of supercooling and frazil ice formation in the laptev sea coastal polynya,
780 J. Geophys. Res., 115, <https://doi-org.uri.idm.oclc.org/10.1029/2009JC005798>, 2010.

781 Drucker, R., S. Martin, and R. Kwok: Sea ice production and export from coastal polynyas
782 in the Weddell and Ross Seas. Geophys. Res. Lett., 38, L17502,
783 <https://doi.org/10.1029/2011GL048668m>, 2011.

784 Fairall, C.W., Bradley, E.F., Hare, J.E., Grachev, A.A., and Edson, J.B.:
785 Bulk parameterization of air sea fluxes: updates and verification for the COARE
786 algorithm, J. Climate, 16, 571-590, [https://doi.org/10.1175/1520-
787 0442\(2003\)016<0571:BPOASF>2.0.CO;2](https://doi.org/10.1175/1520-0442(2003)016<0571:BPOASF>2.0.CO;2), 2003.

788 Fetterer, F., K. Knowles, W. N. Meier, M. Savoie, and A. K. Windnagel. 2017, updated
789 daily. *Sea Ice Index, Version 3*. Sea Ice Index, Version 3. Boulder, Colorado USA.
790 NSIDC: National Snow and Ice Data Center. <https://doi.org/10.7265/N5K072F8>. 09
791 March 2019.

792 Fusco, G., Flocco, D., Budillon, G., Spezie, G., and Zambianchi, E.: Dynamics and
793 variability of terra nova bay polynya, Marine Ecology, 23, 201–209,
794 <https://doi.org/10.1111/j.1439-0485.2002.tb00019.x>, 2002.

795 Fusco, G., Budillon, G., and Spezie, G.: Surface heat fluxes and thermohaline variability in
796 the ross sea and in terra nova bay polynya, Cont. Shelf Res., 29(15), 1887-1895.
797 <https://doi.org/10.1016/j.csr.2009.07.006>, 2009.

798 Gallée, H.: Air-sea interactions over terra nova bay during winter: simulation with a
799 coupled atmosphere-polynya model, J. Geophys. Res-Atmos., 102, 13835–13849,
800 <https://doi.org/10.1029/96JD03098>, 1997.

801 Heorton, H. D. B. S., Radia. N., and Feltham, D. L.: A model of sea ice formation in leads
802 and polynyas, J. Phys. Oceanogr., 47, 1701-1718, [https://doi.org/10.1175/JPO-D-16-
803 0224.1](https://doi.org/10.1175/JPO-D-16-0224.1), 2017.

804 Ito, M., Ohshima, K., Fukamachi, Y., Simizu, D., Iwamoto, K., Matsumura, Y., Eicken, H.:
805 Observations of supercooled water and frazil ice formation in an Arctic coastal
806 polynya from moorings and satellite imagery, Ann. Glaciol., 56, 307-314,
807 <https://doi.org/10.3189/2015AoG69A839>, 2015.

808 Jacobs, S. S.: Bottom water production and its links with the thermohaline circulation,
809 Antarct. Sci., 16, 427-437, <https://doi.org/10.1017/S095410200400224X>, 2004.

810 Knuth, M. A. and Ackley, S. F.: Summer and early-fall sea-ice concentration in the ross
811 sea: comparison of in situ ASPeCt observations and satellite passive microwave
812 estimates, Ann. Glaciol., 44, 303-309, <https://doi.org/10.3189/172756406781811466>,
813 2006.

814 Kurtz, D. D. and Bromwich, D. H.: A recurring, atmospherically forced polynya in terra
815 nova bay in Antarctic Research Series, 43, edited by: Jacobs, S.S., 43, American
816 Geophysical Union, Washington, D.C., 177-201, <https://doi.org/10.1029/AR043p0177>,
817 1985.

818 Lombardo, C., and Gregg, M.: Similarity scaling of viscous and thermal dissipation in a
819 convecting surface boundary layer., J. Geophys. Res., 94, , 6273-6284.
820 <https://doi.org/10.1029/JC094iC05p06273>, 1989.

821 Manwell, J. F., McGowan, J. G., and Rogers, A. L. Wind energy explained: theory, design
822 and application. John Wiley & Sons, West Sussex, England,
823 <https://doi.org/10.1002/9781119994367>, 2010.

824 Martin, S.: Frazil ice in rivers and oceans, Annu. Rev. Fluid Mech., 13(1), 379-397.
825 <https://doi.org/10.1146/annurev.fl.13.010181.002115>, 1981.

826 Martin, S., Drucker, R. S., and Kwok, R.: The areas and ice production of the western and
827 central ross sea polynyas, 1992-2002, and their relation to the B-15 and C-19 iceberg
828 events of 2000 and 2002, J. Marine Syst., 68, 201-214,
829 <https://doi.org/10.1016/j.jmarsys.2006.11.008>, 2007.

830 Mathiot, P., Jourdain, N., Barnier, C., Gallée, B., Molines, H., Sommer, J., and Penduff,
831 M.: Sensitivity of coastal polynyas and high-salinity shelf water production in the Ross
832 Sea, antarctica, to the atmospheric forcing, Ocean Dynam., 62(5), 701-723,
833 <https://doi.org/10.1007/s10236-012-0531-y>, 2012.

834 Matsumura, Y., and Ohshima, K. I.: Lagrangian modelling of frazil ice in the ocean, Ann.
835 Glaciol., 56(69), 373–382, <https://doi.org/10.3189/2015AoG69A657>, 2017.

836 Michel, B.: Physics of snow and ice: morphology of frazil ice, International Conference on
837 Low Temperature Science. I, Conference on Physics of Snow and Ice, II, Conference
838 on Cryobiology, Sapporo, Japan, 14-19 August 1966, Sapporo, Japan, 119–128, 1967.

839 Monin, A. S., and Obukhov, A. M.: Basic laws of turbulent mixing in the surface layer of
840 the atmosphere, *Contrib. Geophys. Inst. Acad. Sci. USSR*, 24, 163-187, 1954.

841 Morales Maqueda, M. A., Willmott, A. J., and Biggs, N. R. T.: Polynya dynamics: a
842 review of observations and modeling, *Rev. Geophys.*, 42(1), RG1004,
843 <https://doi.org/10.1029/2002RG000116>, 2004.

844 Nelson, M., Queste, B., Smith, I., Leonard, G., Webber, B., & Hughes, K.: Measurements
845 of Ice Shelf Water beneath the front of the Ross Ice Shelf using gliders, *Ann. Glaciol.*,
846 58(74), 41-50. doi:10.1017/aog.2017.34, 2017.

847 Nihashi, S. and K.I. Ohshima: Circumpolar mapping of Antarctic coastal polynyas and
848 landfast sea ice: relationship and variability. *J. Climate*, 28, 3650-3670,
849 <https://doi.org/10.1175/JCLI-D-14-00369.1> 2015.

850 Orsi, A.H. and Wiederwohl, C.L.: A recount of Ross Sea waters, *Deep-Sea Res. Pt. II*,
851 56(13), 778-795, <https://doi.org/10.1016/j.dsr2.2008.10.033>, 2009.

852 Ohshima, K.I., Nihashi, S. & Iwamoto, K. Global view of sea-ice production in polynyas
853 and its linkage to dense/bottom water formation. *Geosci. Lett.* 3, 13,
854 <https://doi.org/10.1186/s40562-016-0045-4>, 2016.

855 Ozsoy-Cicek, B., Xie, H., Ackley, S. F., and Ye, K.: Antarctic summer sea ice concentration
856 and extent: comparison of ODEN 2006 ship observations, satellite passive microwave
857 and NIC sea ice charts, *The Cryosphere*, 3(1), 1-9, <https://doi.org/10.5194/tc-3-1-2009>,
858 2009.

859 Park, J., Kim, H.-C., Jo, Y.-H., Kidwell, A., and Hwang, J.: Multi-temporal variation of the
860 ross sea polynya in response to climate forcings, *Polar Res.*, 37(1),
861 <https://doi.org/10.1080/17518369.2018.1444891>, 2018.

862 Petrelli, P., Bindoff, N. L., and Bergamasco, A.: The sea ice dynamics of terra nova bay and
863 ross ice shelf polynyas during a spring and winter simulation, *J. Geophys. Res.-*
864 *Oceans*, 113(C9), <https://doi.org/10.1029/2006JC004048>, 2008.

865 Robinson, N. J., Williams, M. J., Stevens, C. L., Langhorne, P. J., and Haskell, T.
866 G.: Evolution of a supercooled ice shelf water plume with an actively growing subice
867 platelet matrix, *J. Geophys. Res.-Oceans*, 119(6), 3425-3446,
868 <https://doi.org/10.1002/2013JC009399>, 2014.

869 Robinson, N.J., Grant, B.S, Stevens, C.L., Stewart, C.L., Williams, M.J.M. Oceanographic
870 observations in supercooled water: Protocols for mitigation of measurement errors in
871 profiling and moored sampling, *Cold Regions Science and Technology*, 170,
872 <https://doi.org/10.1016/j.coldregions.2019.102954>, 2020.

873 Sansiviero, M., Morales Maqueda, M. Á., Fusco, G., Aulicino, G., Flocco, D., and Budillon,
874 G.: Modelling sea ice formation in the terra nova bay polynya, *J. Marine Syst.*, 166, 4–
875 25, <https://doi.org/10.1016/j.jmarsys.2016.06.013>, 2017.

876 SBE 911plus CTD- SBE 911plus CTD Datasheet: [https://www.seabird.com/profiling/sbe-](https://www.seabird.com/profiling/sbe-911plus-ctd/family-downloads?productCategoryId=54627473769)
877 [911plus-ctd/family-downloads?productCategoryId=54627473769](https://www.seabird.com/profiling/sbe-911plus-ctd/family-downloads?productCategoryId=54627473769), 15 August 2018,
878 2016.

879 Schick, K. E.: Influences of Weather and Surface Variability on Sensible Heat Fluxes in
880 Terra Nova Bay, Antarctica,
881 https://scholar.colorado.edu/concern/graduate_thesis_or_dissertations/m613mx873,
882 2018.

883 Skogseth, R., Nilsen, F., and Smedsrud, L. H.: Supercooled water in an Arctic polynya:
884 observations and modeling, *J. Glaciol.*, 55(189), 43–52,
885 <https://doi.org/10.3189/002214309788608840>, 2009.

886 Smith, M., and Thomson, J.: Ocean surface turbulence in newly formed marginal ice zones,
887 *J. Geophys. Res.-Oceans*, 124(3), 1382-1398, <https://doi.org/10.1029/2018JC014405>,
888 2019.

889 Talley, L.D., Picard, G.L., Emery, W.J. Swift, J.H.: *Descriptive physical oceanography: an*
890 *introduction*, 6, Academic Press, Elsevier, Boston, 2011.

891 Tamura, T., Ohshima, K. I., and Nihashi, S.: Mapping of sea ice production for Antarctic
892 coastal polynyas, *Geophys. Res. Lett.*, 35(7), 1–5,
893 <https://doi.org/10.1029/2007GL032903>, 2008.

894 Tamura, T., K. I. Ohshima, A. D. Fraser and G. D. Williams: Sea ice production variability
895 in Antarctic coastal polynyas, *J. Geophys. Res.*, 121, 2967- 2979,
896 <https://doi.org/10.1002/2015JC011537>, 2016.

897 Thomson, J.: Wave breaking dissipation observed with “swift” drifters, *J. Atmos. Ocean*
898 *Tech.*, 29(12), 1866–1882, <https://doi.org/10.1175/JTECH-D-12-00018.1>, 2012.

899 Thomson, J., Schwendeman, M., and Zippel, S. Wave-breaking turbulence in the ocean
900 surface layer., *J. Phys. Oceanogr.*, 46, 1857–1870, [https://doi.org/10.1175/JPO-D-15-](https://doi.org/10.1175/JPO-D-15-0130.1)
901 0130.1, 2016.

902 Ushio S., and Wakatsuchi, M.: A laboratory study on supercooling and frazil ice production
903 processes in winter coastal polynyas, *J. Geophys. Res.-Oceans*, 98(C11), 20321–
904 20328, <https://doi.org/10.1029/93JC01905>, 1993.

905 Van Woert, M. L.: The wintertime expansion and contraction of the terra nova bay polynya,
906 *Oceanography of the Ross Sea: Antarctica*, Spezie, G. and Manzella, G. M. R.,
907 Springer, Milano, 145-164, https://doi.org/10.1007/978-88-470-2250-8_10, 1999a.

908 Van Woert, M. L.: Wintertime dynamics of the terra nova bay polynya, *J. Geophys. Res.*,
909 104, 7753-7769, <https://doi.org/10.1029/1999JC900003>, 1999b.

910 Vallis, G.: *Atmospheric and oceanic fluid dynamics: fundamentals and large-scale*
911 *circulation*. Cambridge: Cambridge University Press,
912 <https://doi.org/10.1017/9781107588417>, 2017.

913 Weissling, B., Ackley, S., Wagner, P., and Xie, H.: EISCAM — Digital image acquisition
914 and processing for sea ice parameters from ships, *Cold Reg. Sci. Technol.*, 57(1), 49-
915 60, <https://doi.org/10.1016/j.coldregions.2009.01.001>, 2009.

916 Wilchinsky, A. V., Heorton, H. D. B. S., Feltham, D. L., and Holland, P. R.: Study of the
917 impact of ice formation in leads upon the sea ice pack mass balance using a new frazil
918 and grease ice parameterization, *J. Phys. Oceanogr.*, 45(8), 2025–2047,
919 <https://doi.org/10.1175/JPO-D-14-0184.1>, 2015.

920 Worby, A. P., Geiger, C. A., Paget, M. J., Van Woert, M. L., Ackley, S. F., and DeLiberty,
921 T. L.: Thickness distribution of antarctic sea ice. *J. Geophys. Res. - Oceans*, 113(C5),
922 <https://doi.org/10.1029/2007JC004254>, 2008.

923 Zhang, G.: A further study on estimating surface evaporation using monthly mean data:
924 comparison of bulk formulations, *J. Climate*, 10(7), 1592-1600,
925 [https://doi.org/10.1175/1520-0442\(1997\)010%3C1592:AFSOES%3E2.0.CO;2](https://doi.org/10.1175/1520-0442(1997)010%3C1592:AFSOES%3E2.0.CO;2), 1997.

926 Zippel, S. F., and Thomson, J. (2016). Air-sea interactions in the marginal ice zone.
927 *Elementa Science of the Anthropocene*, 4, 95,
928 <http://doi.org/10.12952/journal.elementa.000095>, 2016.

929

930

931 8. ACKNOWLEDGEMENTS

932 We thank Pat Langhorne and one anonymous reviewer for their insightful comments and
933 corrections that have improved this manuscript. This work was supported by the National
934 Science Foundation through NSF Award Nos 1744562 (B. Loose, L. de Pace, URI); 134717
935 (S.F. Ackley, UTSA); 1341513 (E. Maksym, WHOI);1341725 (P.Guest, NPS); 1341606 (S.
936 Stammerjohn and J. Cassano, U Colo). The authors appreciate the support of the University of
937 Wisconsin-Madison Automatic Weather Station Program for the data set, data display, and
938 information.

939

940 9. DATA AVAILABILITY

941

942 The data used in this publication are publicly available from the US Antarctic Program Data
943 Center <http://www.usap-dc.org/view/dataset/601192> and through the CLIVAR Carbon and
944 Hydrographic Data Office <https://cchdo.ucsd.edu/cruise/320620170410>.

945

946

947 10. AUTHOR CONTRIBUTIONS

948

949 LD prepared the manuscript and carried out analyses. MS and JT provided SWIFT data and
950 guidance for upper ocean turbulence analysis. SS prepared and processed the PIPERS CTD data
951 and provided water mass insights during manuscript preparation; SA lead the PIPERS expedition
952 and supported ice interpretations. BL participated in PIPERS expedition, inferred possibility of
953 frazil ice growth and advised LD during manuscript preparation.

954

955 11. COMPETING INTERESTS

956

957 The authors declare that they have no conflict of interest.